Stony Brook University

Improving and Understanding Climate Models: Scale-Aware Parameterization of Cloud Water Inhomogeneity and Sensitivity of MJO Simulation to Physical Parameters in a Convection Scheme

A Dissertation Presented
by
Xin Xie
to
The Graduate School
in Partial Fulfillment of the
Requirements
for the Degree of
Doctor of Philosophy
in
Marine and Atmospheric Science

Stony Brook University

May 2017

Stony Brook University
The Graduate School

Xin Xie

We, the dissertation committee for the above candidate for the
Doctor of Philosophy degree, hereby recommend
acceptance of this dissertation.

Minghua Zhang
Professor, The School of Marine and Atmospheric Sciences, Stony Brook University

Marat Khairoutdinov
Professor, The School of Marine and Atmospheric Sciences, Stony Brook University

Edmund Chang
Professor, The School of Marine and Atmospheric Sciences, Stony Brook University

Andrew Vogelmann
Atmospheric Scientist, Environmental & Climate Sciences Department, Brookhaven National Laboratory

Chris Golaz
Physical Scientist, Lawrence Livermore National Laboratory

This dissertation is accepted by the Graduate School

Charles Taber
Dean of the Graduate School

Abstract of the Dissertation

Improving and Understanding Climate Models: Scale-Aware Parameterization of Cloud Water Inhomogeneity and Sensitivity of MJO Simulation to Physical Parameters in a Convection Scheme

by

Xin Xie

Doctor of Philosophy

in

Marine and Atmospheric Science

Stony Brook University

2017

Microphysics and convection parameterizations are two key components in a climate model to simulate realistic climatology and variability of cloud distribution and the cycles of energy and water. When a model has varying grid size or simulations have to be run with different resolutions, scale-aware parameterization is desirable so that we do not have to tune model parameters tailored to a particular grid size. The subgrid variability of cloud hydrometers is known to impact microphysics processes in climate models and is found to highly depend on spatial scale. A scale-aware liquid cloud subgrid variability parameterization is derived and implemented in the Community Earth System Model (CESM) in this study using long-term radar-based ground measurements from the Atmospheric Radiation Measurement (ARM) program. When used in the default CESM1 with the finite-volume dynamic core where a constant liquid inhomogeneity parameter was assumed, the newly developed parameterization reduces the cloud inhomogeneity in high latitudes and increases it in low latitudes. This is due to both the smaller grid size in high latitudes, and larger grid size in low latitudes in the longitude-latitude grid setting of CESM as well as the variation of the stability of the atmosphere. The single column model and general circulation model (GCM) sensitivity experiments show that the new parameterization increases the cloud liquid water path in polar regions and decreases it in low latitudes.

Current CESM1 simulation suffers from the bias of both the pacific double ITCZ precipitation and weak Madden-Julian oscillation (MJO). Previous studies show that convective parameterization with multiple plumes may have the capability to alleviate such biases in a more uniform and physical way. A multiple-plume mass flux convective parameterization is used in Community Atmospheric Model (CAM) to investigate the sensitivity of MJO simulations. We show that MJO simulation is sensitive to entrainment rate specification. We found that shallow plumes can generate and sustain the MJO propagation in the model.

Table of Contents

List of Figures/Tables/Illustrations

Figure 2.7. (a) Annual mean of global shape parameter distribution diagnosed from CESM simulation using a 2°×2° resolution. (b) same as (a) but assuming global 200 km spatial scale.

Figure 2.8. The adjustment factor in the conversion rate of microphysics scheme with different power relations (y=1, 1.5, 2.5, 3).

Figure 2.9. (a) Cloud fraction from a 5-day simulation from the single column simulation of CAM5. (b) Column-integrated microphysics liquid water conversion difference by using shape parameter ν=0.6, ν=0.8, ν=2.0 and parameterized varying ν relative to the control simulation of ν=1.0. (c) The corresponding varying ν magnitude.

Figure 2.10. (a) Global liquid water path difference between the simulation with varying ν and the control simulation of ν=1.0 (dotted hatch is the area passing the statistical significance test with 95% confidence level). The thick solid line represents the contour of ν=1.0 in the simulation with varying ν. (b) Same as (a) but for shortwave cloud forcing.

Figure 2.11. Annual total precipitation. (a) observation from GPCP. (b)(d) are the output and the difference from GPCP for the control simulation with fixed ν=1. (c)(e) are the output and the difference from GPCP for the simulation with scale-aware parameterized ν. The impact of liquid cloud inhomogeneity is very small compared with the control simulation.

Figure 2.12. Annual total cloud fraction. (a) observation from CLOUDSAT. (b)(d) are the output and the difference from CLOUDSAT for the control simulation with fixed ν=1. (c)(e) are the output and the difference from CLOUDSAT for the simulation with scale-aware parameterized ν. The impact of liquid cloud inhomogeneity is very small compared with the control simulation.

Figure 2.13. Annual total grid-box cloud liquid water path. (a) observation from UWisc. (b)(d) are the output and the difference from UWisc for the control simulation with fixed ν=1. (c)(e) are the output and the difference from UWisc for the simulation with scale-aware parameterized ν.

The negative bias in the control is reduced using varying ν due to the increase of liquid cloud in high latitude.

Figure 3.1. Offline calculation with an average profile from TOGA-COARE. Different colors represents plumes with initial vertical velocoties from 0.1 m/s to 1.4 m/s. (a) Plume MSE (lines in colors), environemtn MSE (solid black line), enviroment saturated MSE (dash line). (b) Entrainment. (c) vertical velocity. (d) Buoyancy. (e) Normalized mass flux (blue line represents the sum of mass flux of all plumes). Dot and cross marks represent properties present in the middle of model level and on the interface respectively.

Figure 3.2. Precipitation (mm/day) simulated in the TOGA-COARE single column run. The black dash line is the observation from TOGA-COARE. (a) and (b) are respectively for CESM default ZM+UW setting and the current convection scheme with the default parameters. All precipitation amount is additive from the components: large-scale precipitation(blue), shallow precipitation (green), and the convective precipitation(red). The precipitation from DEFAULT convection is all considered as deep but it may have shallow components in it.

Figure 3.3. Heating rate contribution only from the convection scheme simulated in the TOGA-COARE single column run. (a) is the observational heating rate from TOGA-COARE including all physical terms. (b) and (c) are for CESM default ZM+UW setting and the current convection scheme with the default parameters.

Figure 3.4. Moisture tendency contribution only from the convection scheme simulated in the TOGA-COARE single column run (unit converted into K/day). (a) is the observational moisture tendency from TOGA-COARE including all physical terms. (b) and (c) are for CESM default ZM+UW setting and the current convection scheme with the default parameters.

List of Abbreviations

ARM - Atmospheric Radiation Measurement

CAM - Community Atmosphere Model

CESM - Community Earth System Model

CRM - Cloud Resolving Model

DOE - Department of Energy

GCM - General Circulation Model

ITCZ - Inter-Tropical Convergence Zone

McICA - Monte Carlo Independent Column Approximation

MICROBASE - the ground-based Climate Research Facility Continuous Baseline Microphysical Retrieval

PDF - Probability Density Function

SST - Sea Surface Temperature

TOA – Top of Atmosphere

Acknowledgments

First, I would like to express my sincere gratitude to my dissertation advisor, Minghua Zhang, for his great support of my Ph.D. study, for his patience, guidance, motivation and immense knowledge. He has constantly given me nice suggestions, cheered me up and helped me refine the manuscript during my writing of this dissertation. I could not have imagined having a better advisor and mentor for my Ph.D. study.

Besides my advisor, I would like to thank the rest of my thesis committee: Prof. Khairoutdinov the committee chair, Prof. Chang, Dr. Vogelmann, and Dr. Golaz, for their insightful comments, encouragement, and enormous help during the time I was doing the dissertation proposal, the time I was writing the dissertation and the defense.

Last but not the least, I would like to thank my parents for supporting me spiritually any time of my life. Finally thank God for giving me so much grace.

Vita, Publications and/or Fields of Study

Xie, X., and M. Zhang (2015), Scale-aware parameterization of liquid cloud inhomogeneity and its impact on simulated climate in CESM, Journal of Geophysical Research: Atmospheres, 120(16), 8359-8371, doi: 10.1002/2015JD023565.

Chapter 1 Introduction

Cloud microphysics and convection parameterizations are two important components of a climate model to simulate cloud processes and the cycles of energy and water in the atmosphere. Cloud microphysics parameterization calculates the sources and sinks of the hydrometeors in the model. An important process in a cloud microphysics scheme is the conversion rates among various cloud hydrometeor species in the atmosphere. The representation of microphysics conversion rate directly determines the distribution and properties of clouds. Since cloud has great impact on the radiation transfer, microphysics can play an important role in changing the energy budget in the climate simulation.

Convection parameterization describes the unresolved subgrid vertical transport within a spatial domain as a result of vertical instability of the atmosphere. It redistributes heat and moisture in a vertical direction. During the ascending or descending motion of the air in convection, microphysical processes such as condensation or freezing takes place. These processes may form clouds, sources and sinks of heat and moisture, leading to precipitation. As a result, the convection parameterization greatly controls the distribution of cloud and precipitation, which is especially significant in the tropics. The heating produced by convection usually has a large impact on many types of atmospheric variability in the tropics such as Madden Julian Oscillation (MJO). Therefore, simulations of clouds, precipitation and atmospheric variability in climate models are greatly impacted by microphysics and convection parameterizations.

1.1 Cloud Subgrid Variability

Because climate models prognostically calculate grid-averaged atmospheric physical variables, subgrid-scale variability need to be parameterized. Early models assumed homogeneous cloud hydrometer distributions within clouds. For example, the radiation in early GCMs was solved by a one-dimensional radiative transfer equation, which assumes that cloud layer is horizontally uniform [*Stephens et al.*, 1991]. However, homogeneous clouds are usually more attenuative relative to more realistic variable cloud with the same optical thickness [*Barker et al.*, 2008]. Later studies showed that the such homogeneity approximation could lead to more than 10% bias in calculating cloud albedo [*Cahalan et al.*, 1994]. Therefore, the impact of subgrid variability on the radiation parameterization has been introduced to provide more accurate radiative flux calculations One way to include this inhomogeneity effect involves describing variable cloud property with a distribution and integrating this PDF. For example, *Barker et al.* [1996] has found that the cloud optical depth distribution over several cloud types could be described by a Gamma distribution so they have proposed a parameterization to correct the homogeneity bias. *Pincus et al.* [1999] suggested that the mean and the dispersion of cloud optical thickness may also depend on cloud types and provide a basis for the subgrid variability parametrization.

An alternative method to introduce subgrid variability is the use of sub column method. The sub column method requires a reconstruction of cloud structure within a grid box so that its sample statistics are consistent with the large-scale cloud variables. *Raisanen et al.* [2004] described a possible way to specify such stochastic cloud structure based on cloud fraction, univariate cloud water amount distribution and a cloud overlap assumption. When a homogeneous radiation calculation could be conducted over each sub column, the total impact given by the averaged flux proved to be more accurate [*Barker et al.*, 1999]. The advantage of a sub column method is that it

could be used with the homogeneous radiative calculation to automatically include subgrid variability impact. However, the computing cost of sub column will be multiplied by the sub column number. To reduce the computing time, *Pincus et al.* [2003] has suggested the Monte Carlo independent column approximation (McICA), which calculates the radiation of a spectral interval only once for a sub column.

Inhomogeneity of cloud properties not only affect radiation calculation, it also impacts cloud microphysics. Microphysics problem is usually represented by two types of models: explicit bin models and bulk parameterization [*Straka*, 2009]. Since GCM has a much larger grid size than LES, the subgrid variability from cloud variables can play a significant role so its impact could not be neglected. Efforts have been made to incorporate inhomogeneity information in the cloud microphysics parameterizations. *Pincus and Klein* [2000] has estimated the impact of subgrid variability in cloud condensate on radiation in both horizontal and vertical directions and they suggested that either tuning or statistical cloud schemes is necessary to account for the impact. *Morrison and Gettelman* [2008] has introduced inhomogeneous cloud liquid amount with a Gamma distribution in their microphysics parameterization. An integration of this Gamma distribution leads to an adjustment factor in the microphysics conversion rates between hydrometeors so that the cloud liquid subgrid variability could be accounted for. *Golaz et al.* [2002] has designed subgrid variability schemes for boundary layer cloud using prognostic probability distribution functions (PDF). *Khairoutdinov and Kogan* [2000] have coupled each model grid with a cloud resolving model so that more subgrid cloud dynamics could be represented.

1.2 Scale Dependence of Cloud Water Inhomogeneity

When subgrid variability is included, it is meant to represent the portion that cannot be resolved within a spatial domain. Observations have shown that the amount of subgrid variability depends

on the domain size, namely the scale of the model grids. When subgrid variability is accounted for in a parameterization, its parameters are usually designed for a fixed domain size. For example, *Khairoutdinov and Kogan* [2000] has emphasized that their proposed bulk microphysics scheme cannot be simply extrapolated for use in large-scale models due to nonlinear dependence of water conversion rates on local cloud variables. If a model resolution changes or a model has different grid sizes, the parameters have to be modified to adapt to different scales. The tuning is tedious so it is desirable that a scale-dependent relationship could be derived from observations. Since currently most climate models do not have such a scale dependence description, it would be also valuable to understand the impact of scale dependence of inhomogeneity in climate model simulation. Early observational cloud subgrid variability was calculated using cloud optical depth. *Barker et al.* [1996] has used Gamma distribution to fit the cloud optical depth derive from 45 Landsat 28.5m resolution images and the subgrid variability represented by Gamma shape parameter has been provided for different cloud types. *Oreopoulos and Cahalan*, 2005] have given a global distribution of subgrid variability for summer and winter using 1°×1 Moderate Resolution Imaging Spectroradiometer (MODIS) data. The comparison of the previous studies indicate the strong dependence of cloud subgrid variability on scale, cloud types and atmospheric conditions [*Shonk et al.*, 2010;*Kawai and Teixeira*, 2011].

The scale dependence of cloud subgrid variability can be described by parameterization so that the calculation in radiation and microphysics can be made scale-aware. *Hogan and Illingworth* [2003] presented ice water content inhomogeneity parameterization with a linear empirical relationship with grid size and vertical shear of the horizontal wind from cloud radar observations. *Hill et al.* [2012] provided another parameterization for the horizontal inhomogeneity of ice water content based on nonlinear relationship on horizontal scales and cloud amount. *Boutle et al.* [2013]

extended the *Hill et al.* [2012]'s formulation to liquid water content and precipitation and showed that such parameterization could correct the microphysics bias significantly.

Climate Research Facility Continuous Baseline Microphysical Retrieval (MICROBASE) value-added product (VAP) is a ground-based observation that provides the primary microphysical parameters of clouds including the liquid/ice water content and liquid/ice cloud particle effective radius [*Johnson et al.*, 2011]. Its high temporal and vertical resolution provides another possibility for cloud subgrid variability study. For the parameterization, previous method has used scale size and cloud fraction as independent variables. As *Kawai and Teixeira* [2011] suggested, atmospheric stability could be candidate too. Alternative observation and parameterization may be worth trying and actual simulation could be conducted to evaluate the scale impact.

Objective 1:

This dissertation aims to understand and parameterize the scale dependence of cloud liquid inhomogeneity by using the observational MICROBASE data. A parameterization of liquid cloud subgrid variability is presented. The observational analysis could be used to verify cloud liquid inhomogeneity parameterization in any model. We have implemented this parameterization in the microphysics scheme of the CESM and investigated its impact on GCM simulations.

1.3 MJO Simulation Sensitivity to Convection Parameters

Madden and Julian Oscillation (MJO) is an intraseasonal oscillation in tropical atmosphere [*Madden and Julian*, 1971]. It is characterized by the planetary convection activities, forming from Indian ocean, propagating eastward at a speed about 3-5m/s, and finally dissipating in the central Pacific ocean [*Zhang*, 2005]. It not only is a remarkable tropical phenomenon but also has wide connections with other components of the climate system, such as Asian-Australian monsoon, ENSO, tropical cyclones, or even extratropical circulation and weather [*WALISER et al.*, 2009].

The MJO simulation in a climate model is one major performance metric of the model, which can have great impact on many other aspects of the model.

It has been reported twenty years ago that most GCMs are not able to capture the intraseasonal oscillation found in the analyses [*Slingo et al.*, 1996]. Despite significant efforts in the community since then to improve the simulation of MJO, many models still fail to simulate MJO. [*Lin et al.*, 2006] showed that only 2 out of 14 models are able to capture the MJO variance close to observations. Many studies have examined the sensitivity of MJO simulation to convective parameterizations. For example, *Khairoutdinov et al.* [2005] has replaced the traditional convective parameterization in each grid with a coupled cloud resolving model, referred to as the super parameterization, and found that this explicit model is able to simulate more realistic MJO. *Li et al.* [2009] found that an artificially lowered latent heating in a climate model may help enhance the eastward propagation. *Zhang* [2005] showed that a convection scheme with a revised closure and a relative humidity triggering could improve the MJO intensity. But it is still not clear what parameters or design of convection parameterization could be the key for realistic MJO simulation. Moreover, few studies have investigated the relative roles of deep and shallow convection in MJO simulations.

The convection parameterization accounts for subgrid variability by describing the impact of an ensemble of convective clouds to the environment. Traditional convection parameterization is usually designed for either shallow convection or deep convection [*Park and Bretherton*, 2009; *Zhang and McFarlane*, 1995]. Recent developments of convection parameterizations have started to include more subgrid varieties of convective plumes so that convections with different heights are described in a unified framework. For example, *Chikira and Sugiyama* [2010] has developed a multiple-plume convection parameterization, in which each plume is specified by an initial

vertical velocity, and the entrainment rate is solved by a parcel lifting equation. In such configurations, both shallow convection and deep convection could be potentially represented consistently. *Park* [2014] has also described a unified multiple-plume convection scheme that aims to simulate dry-moist, forced-free, and shallow-deep convection with a single framework. Improved simulations of MJO have been reported by using such schemes.

Objective 2:

This thesis aims to understand the relative roles of deep and shallow convection in simulating MJO. We implemented a general multi-plume mass flux convective parameterization scheme into the CESM that follows that follows the framework of *Arakawa and Schubert* [1974] and *Chikira and Sugiyama* [2013]. The scheme is general and flexible enough to investigate the sensitity of MJO simulations to key processes in a convective parameterization. Our effort is not directed to improve the overall performance of climate simulation in the CESM. Instead, it is to understand the sensitivity of MJO simulations to physical assumptions under the framework of the multi-plume convective parameterizations.

1.4 Outline

This dissertation is organized into two major chapters. Chapter 2 describes our finding for the scale dependence of cloud liquid inhomogeneity by using observational data. A parameterization was proposed and evaluated in CESM model. This chapter has been published as *Xie and Zhang* [2015]. Chapter 3 is the investigation of MJO sensitivity to several convection parameters and options. A multiple-plume is implemented into CESM and used as a tool to understand the model sensitivity. The last chapter summarizes the conclusions and describes future work.

Chapter 2 Scale-aware Liquid Cloud Inhomogeneity Parameterization for the CESM

2.1 Motivation

The physical parameterizations of subgrid processes are crucial for realistic climate simulation in climate models. They are usually designed based on physical assumptions with empirically determined parameters. Because the subgrid processes depend on the size of the model grids, these parameters need to be tuned for different resolutions of the model. Tuning a model is not only tedious, but also difficult when variable resolutions of drastically different grid sizes need to be used, such as the regional refinement of grids [*Taylor et al.*, 2008]. Therefore, it is of great interest to develop scale-aware parameterizations to make them resolution independent.

The subgrid variability of cloud hydrometers is known to impact radiation and microphysics processes in climate models. It was introduced into the general circulation models (GCMs) in *Cahalan et al.* [1994] and *Barker* [1996] to correct the radiation flux biases over horizontally inhomogeneous clouds. Relative to homogeneous clouds, the subgrid-scale variability of cloud water reduces the grid-averaged albedo of solar radiation. The larger the inhomogeneity of cloud water within a grid cell, the more efficient the autoconversion and accretion of liquid water to rainwater because of the nonlinear dependence of the conversion rate on liquid water content [*e.g.*, *Morrison and Gettelman*, 2008]. Several types of methods have been used to describe the subgrid variability of cloud water in large-scale models. Some studies represented it with the sub column method, which statistically reconstructs the internal cloud structure by using large-scale cloud fraction information and overlapping assumption [*Jakob and Klein*, 1999; 2000; *Jess et al.*, 2011; *Pincus and Stevens*, 2009; *Pincus et al.*, 2003; *Pincus et al.*, 2006; *Raisanen et al.*, 2004]. Other

studies sought to specify the assumed probability density function (PDF) of cloud quantities diagnostically or prognostically [*Bogenschutz and Krueger*, 2013; *Golaz et al.*, 2002; *Larson and Golaz*, 2005; *Norris et al.*, 2008; *Tompkins*, 2002] so that the subgrid variability effect can be accounted by integrating the cloud PDF for microphysics [*Larson and Griffin*, 2013; *Pincus and Klein*, 2000; *Weber and Quaas*, 2012; *Wood et al.*, 2002] and for radiation calculations [*Shonk and Hogan*, 2008; 2010; *Shonk et al.*, 2010].

Previous studies have pointed out the strong dependence of subgrid variability on the horizontal scale and other atmospheric conditions. However, few studies have investigated how to quantitatively describe these dependences. *Pincus et al.* [1999] related the cloud subgrid variability to the underlying cloud types. *Oreopoulos and Cahalan* [2005] gave a very comprehensive survey for the 1°×1° global cloud inhomogeneity climatology including latitudinal, seasonal, and diurnal change using MODIS data. *Kawai and Teixeira* [2011] examined the probability density function of marine boundary layer clouds and pointed out its implications for cloud parameterization. These studies provided very valuable observational base to formulate cloud inhomogeneity, even though they did not directly derive the cloud inhomogeneity parameterizations for large-scale models. *Hogan and Illingworth* [2003] was the first study that described a linear empirical relationship of ice water content inhomogeneity with grid size and vertical shear of the horizontal wind from cloud radar observations. *Hill et al.* [2012] provided another parameterization for the horizontal inhomogeneity of ice water content based on nonlinear relationship on horizontal scales and cloud amount. *Boutle et al.* [2013] extended the *Hill et al.* [2012] formulation to liquid water content and precipitation. These two recent parameterizations used both cloud fraction and horizontal scale as the predictor variables. Our study differs from theirs by including other meteorological conditions.

According to *Kawai and Teixeira* [2011], the in-cloud liquid inhomogeneity should also depend on atmosphere instability, which will be used in the parameterization derivation of this study.

The objective of this study is to use the long-term high-resolution data of cloud water from the Department of Energy (DOE) Atmospheric Radiation Measurement (ARM) program at different latitudes to develop a scale-aware parameterization of cloud water inhomogeneity on resolved atmospheric instability. A second objective is to understand the impact of the parameterization on the simulated climate by the Community Earth System Model (CESM). Recently, *Huang et al.* [2014] used the same dataset to study the standard deviation, relative dispersion (the ratio of the standard deviation to the mean), and skewness of cloud liquid water. They reported the dependence of these parameters on the length of the averaging time. Our work differs from their study in that we focus on the dependences on the spatial length scale and the atmospheric conditions, and we target them for parameterizations in large-scale models. An outline of this study is as follows. Section 2.2 describes the observational data and methods that we use to estimate the liquid cloud inhomogeneity. Section 2.3 shows the relationship of the cloud inhomogeneity parameter with scale, location, and season. A parameterization is presented. Section 2.4 presents the results of the impact of the new parameterization in CESM single column and General Circulation Model (GCM) experiments via the autoconversion and accretion microphysics processes. Section 2.5 contains a summary.

2.2 Data and Model

This study uses the ground-based Climate Research Facility Continuous Baseline Microphysical Retrieval (MICROBASE) value-added product (VAP) developed by ARM [*Johnson and Jensen*, 2011]. MICROBASE combines measurements from 35-GHz millimeter wavelength cloud radar, ceilometer, micropulse lidar, microwave radiometer, and balloon-borne

radiosonde soundings to produce cloud water vertical profile [*Johnson et al.*, 2011]. Its latest version MICROBASEPI2 provides instantaneous liquid water content profile in 10 second time intervals and 512 vertical levels, each layer 43m thick. The resultant temporal resolution is sufficient to capture the small-scale cloud profile for the present study of cloud variability. The quality control flags supplied by the product classify the liquid data into bad, indeterminate, and good categories. The good flag has excluded many questionable measurements, for example liquid water content out of normal range or with precipitation contamination, so only the liquid water content data with good quality flag are used in this study. As a common problem for cloud radar reflectivity data, drizzle may introduce positive bias to liquid water content in lower altitude and this could result in some uncertainty in parameterization derivation. But since we use the ratio of cloud water content mean to its variance (shown later in Equation (2.2)), the error introduced by incorrect scaling should be small. Because our focus is only on in-cloud liquid inhomogeneity, only data with liquid water content greater than zero are used. Data from the ARM sites at Barrow (NSA C1), Lamont (SGP C1), and Darwin (TWP C3) are selected to represent high, middle, and low latitudes respectively. To demonstrate the capability of MICROBASEPI2 dataset, Figure 2.1 gives two examples of short-term MICROBASEPI2 temporal variation of liquid water content above two of the ARM sites. Figure 2.1 (a) shows middle and low clouds at SGP C1, while Figure 2.1 (b) shows deep convective clouds at TWP C3. With the high temporal 10s resolution, the data reveal more small-scale details in the liquid cloud distributions.

To study the spatial scale dependence of liquid cloud inhomogeneity, the ground-based MICROBASE cloud measurements in temporal coordinate cannot be used directly. We assume ergodicity of clouds or Taylor hypothesis so that the spatial variability can be deduced with the cloud data and wind data combined. *Grützun et al.* [2013] suggested that the ergodicity assumption

of ground-based remote sensing data may introduce bias for cloud spatial variability studies within a short time period. Therefore, we used three years of long-term data (from 2008-2010) in this study to alleviate possible bias. Wind velocity from the ARM Best Estimate Data Product [*Xie et al.*, 2010], with vertical resolution 45m and 6 hour temporal interval is integrated at each vertical level to calculate what distance the cloud field has moved. This transformation converts the temporal variation into spatial distribution.

In spatial coordinate, we quantify the in-cloud liquid cloud inhomogeneity by using the shape parameter ν of a Gamma distribution at different spatial scales. The same Gamma distribution is used in the cloud microphysical scheme of CESM [*Morrison and Gettelman*, 2008] to calculate the auto-conversion and collision-coalescence processes of cloud droplets with a specified value of 1.0 for the shape parameter. A Gamma distribution is assumed because it has been found to fit observational cloud water well [e.g., *Barker et al.*, 1996; *Huang et al.*, 2014]. The Gamma distribution is written as

$$P(q) = \frac{1}{\Gamma(\nu)} \frac{1}{\theta^{\nu}} q^{\nu-1} e^{-\frac{q}{\theta}} \tag{2.1}$$

where ν is the shape parameter and θ is the scale parameter. The shape parameter ν in the Gamma function can be written as

$$\nu = \frac{\bar{q}^2}{\sigma^2} \tag{2.2}$$

where σ^2 is the variance of in-cloud liquid water mixing ratio q and $\bar{q}$ is the mean of q. The shape parameter ν of liquid water is calculated using maximum likelihood method (MLE) [Thom, 1958] from the MICROBASE data for clouds of different spatial scales (including both clear-sky and cloudy conditions). Every four vertical levels of MICROBASE data are combined into one level, in order to obtain more liquid samples to do distribution estimation. The ARM Best Estimate

Dataset (ARMBE) is also used in the derivation of the parameterization to understand which atmospheric condition controls ν. Figure 2.2 shows two snapshots of the estimated shape parameters that have been converted to spatial coordinates given various scales corresponding to the profile from the first few hours at the SGP C1 and TWP C3 sites in Figure 2.1. The shape parameter is generally small (larger inhomogeneity) at the edge of the thick clouds where strong mixing of cloudy and environment air happens. This is expected because entrainment produces more variation in cloud hydrometer properties. The increased variability, which is the denominator of the shape parameter (Equation (2.2)), lowers the shape parameter. In the thick cloud core, where cloud liquid content is relatively homogeneous, a large shape parameter is usually seen (see Figure 2.2 (b)(d)).

Note that several other measures could be used to characterize cloud inhomogeneity, for example, inhomogeneity parameter χ [Oreopoulos and Cahalan, 2005] or fractional standard deviation f [Boutle et al., 2013; Hill et al., 2012]. These parameters are generally comparable and can be converted to each other [Shonk et al., 2010]. The reason we use the definition of inhomogeneity in terms of ν in this study is that CESM also uses ν to represent liquid cloud inhomogeneity in the microphysics conversion process [Gent et al., 2011; Morrison and Gettelman, 2008]. We are interested in implementing the scale-aware parameterization of ν in CESM and investigate its impact on simulated climate. We also use the single column version of CESM to analyze the impact. In the single column setting, we run a short simulation at SGP C1 to evaluate the direct impact of ν on simulated cloud water without its interactive effect on radiation and microphysics. In the GCM configuration, we run the CESM standalone atmospheric model CAM5 with prescribed climatological Sea Surface Temperatures (SST) at a 2° longitude-latitude grid with the finite volume dynamical core. Since the longitude-latitude grid in CESM has larger (smaller)

horizontal grid over equator (polar region), the scale impact of the parameterization could be investigated. We run each simulation for 4 years and analyze the results from the last 3 years.

2.3 Parameterization of the Shape Parameter

2.3.1 Shape Parameter Dependence on Scales and Atmosphere Instability

At each location and height, the frequency distribution of the in-cloud liquid water is obtained from the high-resolution data within the given scale. Figure 2.3(a) to Figure 2.3(c) show the examples of the frequency distribution at SGP C1 and at 100 meter height for three different horizontal scales (5 km, 25 km, and 100 km respectively) at about 02Z on June 3, 2009. Also plotted is the fitted Gamma distribution (dash lines) using MLE. It can be seen that the Gamma distributions capture the shape of the observed liquid water content histogram well. We can also see that the estimated shape parameter from the fitting decreases (from 5.18 to 2.17) with the increasing horizontal scales (from 5 km to 100 km). This is because a spatial segment of larger scale tends to cover more cloud regimes so it includes more liquid inhomogeneity than a smaller scale. Therefore, larger scales are associated with larger variance of liquid water for given mean liquid water, so they are associated with smaller shape parameter (shown later in Equation (2.4)). Smaller scales, however, may just cover a portion of a large cloud. They are associated with larger shape parameter. As the scale approaches zero, the variance of liquid water will approach zero, which is associated with an infinite shape parameter.

We calculated the shape parameters for different sites (NSA C1, SGP C1, and TWP C3), different seasons (December-January-February (DJF) and June-July-August (JJA)), and different scales (from 5 km to 200 km). The median values at each height are shown in Figure 2.4 by the dense lines, with the three locations given in the three rows, the two seasons given in the two columns, and the various scales in different colors. Several features are noted. The first is the

consistent decrease of the shape parameter with increasing horizontal scales in almost all the panels. The decrease is not linear. For example, in Figure 2.4(a), the shape parameter changes from around 5 to 2 for small scales from 5 km to 50 km while for larger scales from 50 km to 200 km, the change is only from 2 to 1.

The second feature in Figure 2.4 is that ν depends strongly and consistently on season and location. At NSA and SGP, ν in JJA is systematically smaller than its magnitude in DJF, meaning more inhomogeneity in the warm season. From the high-latitude NSA C1 to the low-latitude TWP C3, the shape parameter has a decreasing trend. This is because the low-latitude warm atmosphere is more frequently associated with more unstable atmospheric condition and convective clouds than the high-latitude and cold atmosphere, thus it has larger inhomogeneity and smaller shape parameter. The dependence of season and location here is consistent with the results of *Kawai and Teixeira* [2011]: more cloud inhomogeneity in warm season; less inhomogeneity in cold season. Based on these observations, we combine the shape parameter dependences on season and location into one single variable, atmosphere instability, for any given scale.

There is also a height dependence of the shape parameter in Figure 2.4. For example, there is a linear increase of shape parameter with height in Figure 2.4(e). However, no generalized relationships with height can be derived for all stations. We therefore neglect the height dependence of ν, acknowledging that this can be improved in the future.

2.3.2 Parameterization

A simple metric of atmosphere instability can be defined as

$$S = \frac{h_{950} - h_{500}^{*}}{45000Pa} \tag{2.3}$$

, where h_{950} is the moist static energy at 950hPa and h_{500}^{*} is the saturated moist static energy at 500hPa. This formula is an approximate measure of convective available potential energy (CAPE)

but its simplicity allows for easy calculations [*Arakawa and Schubert*, 1974]. Usually, the larger the S, the more unstable the atmosphere is. This instability parameter is calculated using the data from ARMBE. When S is negative, the atmosphere is stable. S is a crude measure of the atmospheric stratification.

According to the studies of *Boutle et al.* [2013] and *Hill et al.* [2012], the nonlinear dependence cloud inhomogeneity on scale could be described by a -5/3 power law relationship. In their papers, cloud inhomogeneity is represented by fractional standard deviation $f = \sigma/\bar{q}$, which is proportional to $x^{1/3}$ (x is length scale). We follow their proposed scale power function in this study. Since we use shape parameter ν to represent inhomogeneity here, the relationship of $\nu = 1/f^2$ implies that the equivalent scale power function for ν is $x^{-2/3}$. Multivariate regression was then used to find the best fit of ν as a function of the scale $x^{-2/3}$ and the atmosphere instability S at the three latitudes and in the two seasons. We arrived at the following formula

$$\nu = 0.67 - 0.38 \cdot S + 4.96 \cdot x^{-\frac{2}{3}} - 8.32 \cdot S \cdot x^{-\frac{2}{3}} + R(x, S) \qquad (2.4)$$

where the horizontal scale x is in kilometer; S is atmospheric instability given in Equation (2.3) in unit J/kg/Pa, R is a stochastic parameter to represent the uncertainties of the ν values from cloud variability, including the sampling errors and the imperfectness of the formula. We note that the two dependent parameters and the form of the parameterization are only heuristically determined because of the inherent complexities of the cloud variability. This formula is plotted in Figure 2.5(a) with S as the abscissa and the scale as the ordinate with $R(x, S)$ set to zero. As expected, shape parameter decreases with increasing horizontal scale and increasing atmospheric instability. Figure 2.5(b) shows the binned mean of shape parameter from observation. It is seen that Equation (2.4) captures the major pattern of ν variations in observations, especially for scales smaller than 90 km. It may underestimate ν at large scales slightly (in the upper region of the figure) compared

with the binned observational mean but this is still within the observational range. The standard deviation of the random term $R(x,S)$ is shown in Figure 2.5(c).

To further investigate whether the parameterization can reflect the realistic variability of shape parameter in observation, we used Figure 2.6(a)-(d) to show the shape parameters from the instantaneous observations against the corresponding values from the parameterization with the stochastic term set to zero, for different given scales. For three years of data, we have collected the lower quartile, the median, and the upper quartile of the instantaneous ν respectively in each month and calculated the parameterized ν based on the collocated instability and spatial scale using Equation (2.4). In these figures over selected horizontal scales, the observational shape parameters (shown as dots) exhibit a significant decrease with larger instability (more unstable atmosphere), which is well captured by the derived parameterization shown in solid black line. The scale dependence is also evident. The overall magnitude of ν changes from about 1.0 for 200 km to about 4.0 for 10km (see Figure 2.6(a) and (d)) and the parameterization lies within the observational range. The unresolved variability is represented by the residual term $R(x,S)$ in Equation (2.4), which is shown in Figure 2.5(c). When the shape parameter is used in the microphysical parameterization, this residual term can either be set to zero or treated stochastically to represent the uncertainties.

2.4 Impacts on Climate Simulation

The proposed parameterization is next implemented in CESM for the calculation of cloud microphysics. In the global model, at the location where the surface pressure is lower than 950hPa, h_{950} is replaced by the surface moist static energy and the denominator is replace by $(P_s - 500hPa)$ in Equation (2.3). Figure 2.7(a) shows the global distribution of the annual mean shape parameter diagnosed from CESM simulation of 2°×2° resolution. It is seen that ν gradually

increases from about 0.7 in the equatorial regions to up to 5.0 in the polar regions. This is consistent with the longitude-latitude grid size distribution in CESM, where the larger low-latitude grid size contains more inhomogeneity (lower ν) and vice versa. Along the same latitude band, atmosphere instability also plays a significant role in varying ν, especially in tropics. The area with lower ν generally matches the region with high SST and convective clouds, such as Tropical West Pacific Warm Pool, the Pacific ITCZ, and the Atlantic ITCZ.

Some previous studies also provided the map for the global distribution of ν [*Lebsock et al.*, 2013; *Oreopoulos and Cahalan*, 2005]. The spatial pattern of our parameterized shape parameter is consistent with *Lebsock et al.* [2013], where major tropical oceans usually have lower ν and high latitudes have larger ν (see their Figure 6). The magnitude of our parameterized ν is overall smaller than most previous studies based on satellite data [*Barker*, 1996; *Boutle et al.*, 2013; *Cahalan et al.*, 1994; *Lebsock et al.*, 2013; *Oreopoulos and Cahalan*, 2005]. In Table 2.1, we compared the cloud inhomogeneity parameter values and the different sampling methods from these studies as summarized by *Shonk et al.* [2010] with our study. The relatively smaller value in our study is likely because we used radar data at high temporal and vertical resolutions while these studies used satellite cloud optical depth data. Higher frequently sampling captures more cloud variability and may introduce larger variance σ^2 therefore causing smaller ν ($\nu = \bar{q}^2/\sigma^2$). Our result is comparable to *Barker* [1996] (Table 2.1), which uses LandSat data with 0.04km sampling resolution, higher than other satellite studies in the table. In addition, the larger grid box size using a CESM 2°×2° grid in our study is mostly larger than the horizontal scale in their estimations (see Table 2.1). Therefore more inhomogeneity and smaller ν is expected from our calculation.

In the microphysical scheme of CESM, prior to version 1.2.0 [*Morrison and Gettelman*, 2008], ν was set as 2.0, which is close to the overall mean ν from *Lebsock et al.* [2013] and *Oreopoulos*

and Cahalan [2005]. It has been changed to 1.0 in the publicly released default model of CESM version 1.2.0, closer to our estimation. From Figure 2.7(a), we can see that the parameterized ν could be from about 0.7 with 200km gridbox over an equatorial unstable atmosphere to about 5.0 with a much smaller grid box at the polar region. Therefore, according to the parameterization, the default fixed value 1.0 overestimates ν at low latitudes but underestimates it at high latitudes. The use of uniform spatial sizes in a climate model may greatly reduce such large cloud inhomogeneity difference due to scale dependence. We have also included a map of ν distribution assuming global constant spatial scale 200km in Figure 2.7(b) to emulate such a uniform grid. Note that the color range in Figure 2.7(b) is a much smaller than that in Figure 2.7(a). The spatial variation of ν in Figure 2.7(b) is entirely due to changes in atmospheric conditions. ν is still larger at highs latitudes, but the latitudinal gradient of ν is reduced.

As has been pointed out in many previous studies [*e.g., Huang and Liu*, 2014; *Lebsock et al.*, 2013], the shape parameter ν can impact the conversion rates in the sinks of the cloud liquid water. When the sink terms *S* is expressed as liquid water mixing ratio q_l to the power of y as $S \propto (q_l)^y$, the subgrid variability effect can be described by multiplying the conversion rate with an adjustment factor [*Morrison and Gettelman*, 2008]:

$$E = \frac{\Gamma(\nu + y)}{\Gamma(\nu)\nu^y} \tag{2.5}$$

Figure 2.8 shows how the adjustment factor changes with ν within commonly used y range (from 1.0 to 3.0) in the microphysical schemes. Compared with the globally fixed shape parameter 1.0 in the default CESM, a ± 0.5 change of shape parameter around 1.0 could introduce about $\pm 20\%$ change to the original adjustment factor given $y = 1.5$ and more than about $\pm 120\%$ change given $y = 3$. In CESM, the major nonlinear conversion terms in the liquid water tendency equation are from the rain autoconversion and accretion processes, with y values of 2.47 and 1.15

respectively [*Khairoutdinov and Kogan*, 2000; *Morrison and Gettelman*, 2008]. Therefore, compared with the fixed ν 1.0 case, the parameterized ν will lead to higher conversion rate from cloud liquid to rain in the low latitudes ($\nu < 1.0$) and lower conversion rate in the higher latitudes ($\nu > 1.0$).

2.4.1 Single Column Simulation

We first use a single column simulation to demonstrate the direct impact of ν on CESM microphysics processes. The simulation uses ARM SGP forcing data starting on 07/19/1995 for five days. The control run uses CESM default setting with the fixed $\nu = 1.0$. Figure 2.9(a) shows the cloud fraction distribution from the control run. Convection developed at day 1.5, so significant microphysical conversion from liquid cloud to precipitation is expected at that moment. Focusing on this short period of vigorous cloud activity, we carried out the offline microphysics calculation with $\nu = 0.6$, $\nu = 0.8$, $\nu = 2.0$ and the CESM $2° \times 2°$ grid scale. The interactive effect of ν is suppressed by using the liquid water from the control run in the radiation and in the subsequent microphysical calculations. The lines in Figure 2.9(b) show the liquid water conversion difference within each time step between the sensitivity simulations and the one from the control run. As expected, the simulations with ν smaller than 1.0 shown by dotted line ($\nu = 0.6$) and dash dot line ($\nu = 0.8$) have larger liquid water sinks (more negative tendency). But the one with $\nu = 2.0$ has more liquid water due to smaller liquid water conversion. The difference in the liquid water tendency from the simulation using the parameterized ν is shown by a solid line. It is between the lines using $\nu = 0.6$ and $\nu = 0.8$ at the peak. The corresponding ν is plotted in Figure 2.9(c) as the thick line that fluctuates around 0.7. These are all consistent with the expectation that smaller ν, corresponding to large inhomogeneity of liquid water, is associated with larger cloud-to-rain conversion rate, and less cloud water, while the opposite is true for larger ν.

2.4.2 GCM Simulation

We next show the sensitivity of the cloud liquid water to the varying ν using a GCM simulation. Instead of fixing liquid water content and diagnosing its converting tendency offline, we calculated the parameterized shape parameter ν at each grid point of CESM and allowed it to impact the microphysics processes in the *Morrison and Gettelman* [2008] cloud microphysical scheme. The liquid water content will respond to the modified cloud liquid conversion rates so liquid cloud distribution will be changed which will in turn impact the model hydrological and dynamical processes. We have run CESM in a 2°×2° resolution for four years and the following analysis is based on the annual mean of the last three-year results. In the CESM longitude and latitude grid setting, the 2°×2° resolution corresponds to spatial grid scale ranging from over 200 kilometers near the Equator to about 5 kilometers in the polar region. Owing to the interactive nature of the cloud microphysics and radiation, the response is not expected to be the same as the direct impact of ν in the offline simulation.

Figure 2.10 (a) shows the difference of the annual liquid water path between the simulation with varying ν and the control run with fixed $\nu = 1.0$. The black thick line shows the contour of $\nu = 1.0$. The hatched areas pass Student t-test with the confidence level 95%. It is seen that even though the interactive response is very noisy, at higher latitudes where $\nu > 1.0$, there is an overall increase of cloud liquid water path; in the middle and low latitudes, cloud liquid water is overall reduced. We have calculated the area average of these differences in both high latitudes (poleward of 45°) and low latitudes (equatorward of 45°). The area-averaged liquid water path is increased by 0.43g/m^2 in high latitudes and decreased by 0.82 g/m^2 in low latitudes. These represent about 1.4% increase and 1.7% of decrease of the cloud water path in the control simulations.

The distribution change of liquid water content is expected to impact radiation. Because the parameterization in this study only affects warm liquid clouds, the radiative impact is expected to be most clear in the regions of low clouds. Figure 2.10(b) shows the shortwave cloud forcing difference between varying ν and control $\nu = 1$. The local response is generally consistent with the liquid cloud content change, where liquid increase corresponds to stronger shortwave cloud forcing, and liquid decrease corresponds to weaker shortwave cloud forcing. While the figure is noisy, in the subtropical eastern Pacific where low clouds dominate and ν is larger than 1, shortwave cloud forcing is more negative. The difference is about 5 W/m^2. In the Arctic, where we have smaller grid size, larger ν, and generally less efficient liquid cloud conversion, the region passing the statistical significance test has less negative shortwave cloud forcing with a difference up to 5 W/m^2.

When averaged over the globe, we have found that the varying ν has relatively small impact on the overall climate. Since the contour with $\nu = 1$ is around 30S and 30N, compared to the control run with all constant $\nu = 1$, the varying ν case here produces opposite impacts over low and high latitude on the shape parameter distribution and further causes opposite microphysics and radiation impacts. It is possible these opposing impacts in the tropics and the Arctic may cancel each other. Besides liquid cloud distribution and radiation, the shape parameter ν is expected to impact precipitation because it adjusts the efficiency of liquid cloud autoconversion and accretion processes to large scale precipitation. Annual total precipitation for the varying ν and control versions compared with observation from Global Precipitation Climatology Project (GPCP) are presented Figure 2.11. The control CESM version has a global mean at about 3mm/day and it shows a spurious double Inter-Tropical Convergence Zone (ITCZ) and too much precipitation over Indian ocean. However, the version with varying ν exhibits almost the same precipitation pattern

as the control version. In CESM, the precipitation in tropics is dominated by convective process so the rainfall distribution is less affected by the liquid cloud conversion in microphysics scheme. At high latitudes, where the subgrid variability adjustment is large, the magnitude of precipitation is generally small to see such scale impact. We also compared the total cloud distribution of these two versions with CloudSat cloud observation in Figure 2.12. The impact of varying ν versus the control is small. The annual liquid water path shown in Figure 2.13 presents a slight improvement using varying ν than the control. This is because the less subgrid variability in high latitude converts liquid less efficiently so the negative bias in the control is reduced. This also suggests that the default model is nearly optimally tuned. However, the impact of the parameterized ν on a model with different resolutions may be larger if the shape parameter is not optimally tuned. For example, if we increase the model resolution to 1°, we expect that the shape parameter ν will increase globally and cause weaker liquid cloud autoconversion and accretion. This may generally increase the global large scale liquid water path and reduce shortwave cloud forcing.

2.5 Conclusion

We analyzed the long-term ground-based MICROBASE dataset to derive the liquid cloud inhomogeneity represented by the shape parameter ν of the Gamma distribution. Smaller ν is associated with larger inhomogeneity. We reported the dependence of ν on the horizontal scale and atmospheric instability and derived a scale-aware parameterization of ν that depends on the model resolution and atmospheric state.

When the parameterization is implemented in CESM at a $2^{o}\times2^{o}$ resolution, we found that the inhomogeneity parameter ν is larger than the default value of $\nu = 1$ in high latitudes and smaller than the default value in low latitudes that is used in CESM, owing to the varying grid sizes and atmospheric instability. Larger values of the parameter are shown to correspond to more cloud

liquid water, owing to smaller rate of cloud-to-rain conversion. Smaller values of the parameter ν lead to less cloud water in the simulation. The parameterized inhomogeneity therefore leads to more cloud water in high latitudes. However, the overall impact of the parameterization on the default model is small, owing to the fact the default model used a tuned parameter that is close to the observationally derived values.

This study is only a small step toward the scale-aware description of cloud water inhomogeneity. Future studies should include cloud ice and other hydrometeors. While the impact of the parameterized inhomogeneity on the simulated climate in this study is small, we think the main benefit of the scheme is its direct use in variable resolution models.

Tables

Table 2.1. Comparison of Cloud Inhomogeneity Parameters in Previous Studies[a]

Reference, source	Observational Property	Effective Spatial Resolution	Gridbox Size	Estimation Method	Mean of equivalent ν
Barker [1996], LandSat	cloud optical depth	0.04 km	58 km	MOM	1.5
Oreopoulos and Cahalan [2005], MODIS	cloud optical depth	2 km in middle latitude and 5 km in equator	1°×1°, 45 km in middle latitude and 110 km in equator	MLE and MOM	2.96 in Jan and 2.87 in Jul
Lebsock et al. [2013], CloudSat and MODIS	cloud water path	1.1km	141 km	MOM	2.46
Parameterization in this study, MICROBASE	liquid water content	0.01 km to 0.1 km for wind speed 1 m/s to 10 m/s	2°×2°, 90 km in middle latitude and 220 km in equator	MLE	1.1

[a] The references may have different inhomogeneity definition usually estimated by either MOM (method of moments) or MLE (maximum likelihood estimation) but we have converted them to the equivalent Gamma shape parameter ν.

Figures

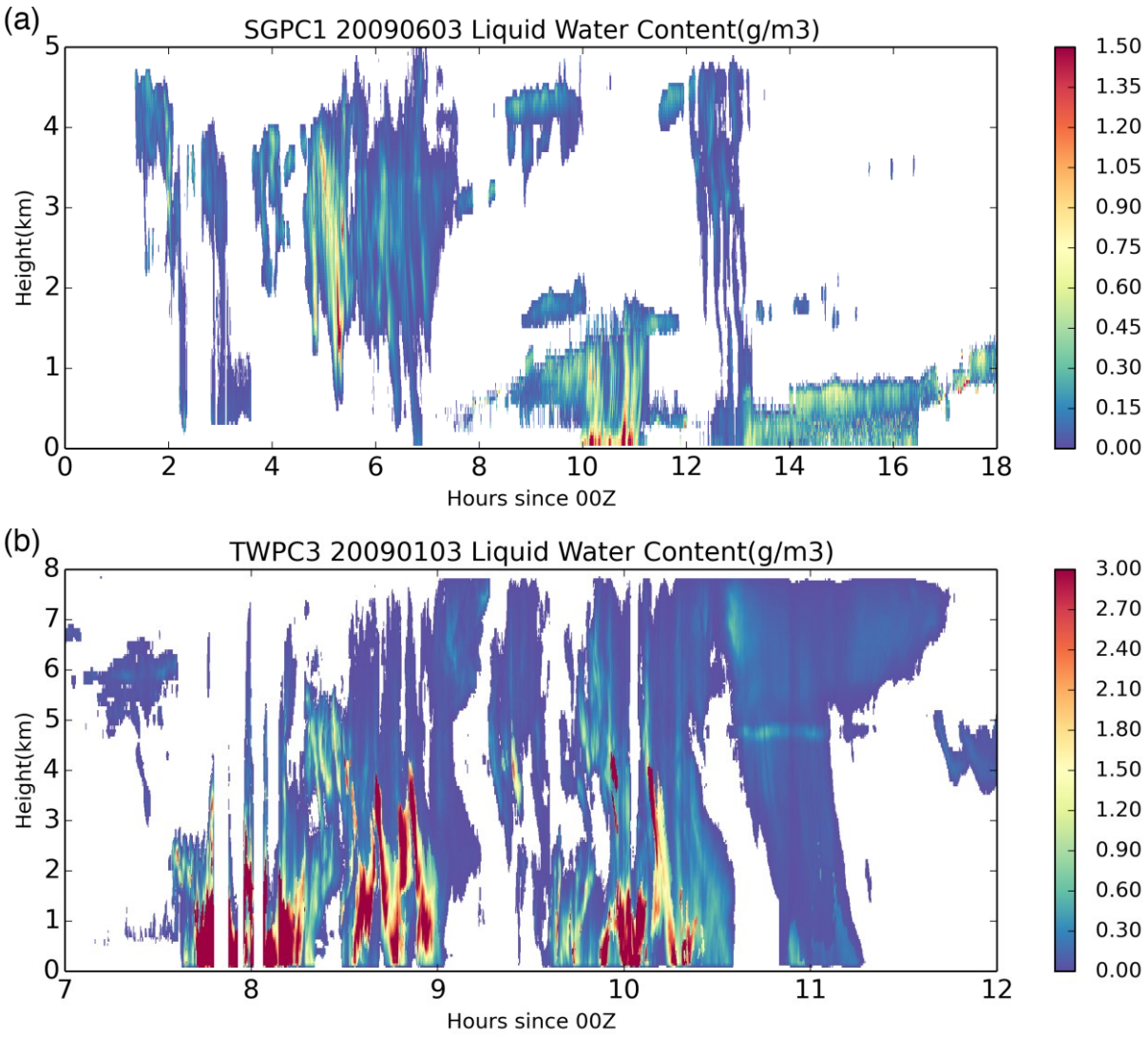

Figure 2.1. (a) An example of MICROBASEPI2 liquid water content profile on 06/03/2009 at SGP C1 site. (b) Same as (a) but at TWP C3 site on 01/03/2009.

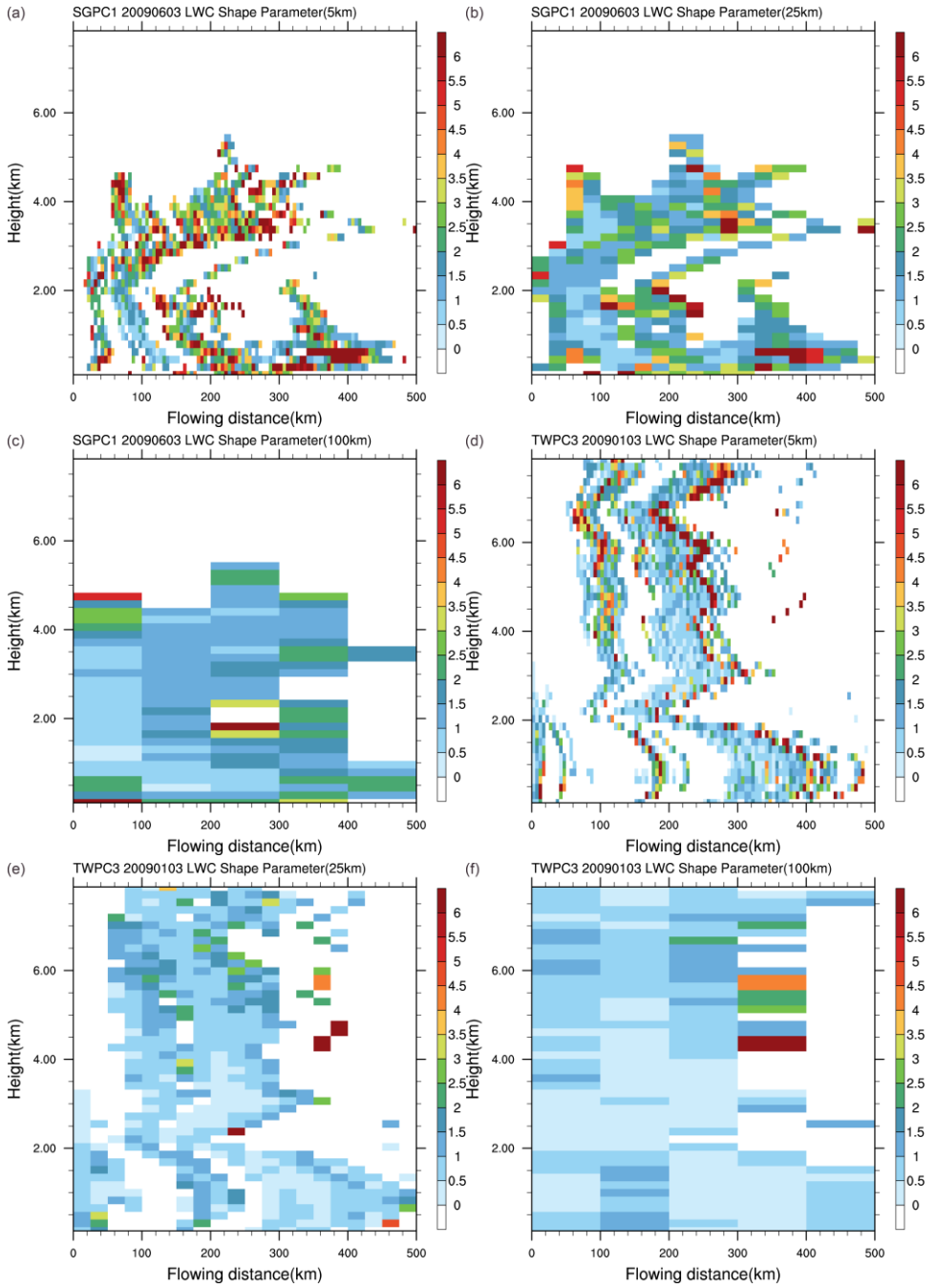

Figure 2.2. (a-c) snapshot of liquid cloud shape parameter at SGP C1 site on 06/03/2009 estimated in given spatial scales 5km, 25km, and 100km. These data are converted from temporal ground observation combined with wind information. Flowing distance represents the spatial coordinate converted from temporal coordinate. (d-f) are as for (a-c) but for TWP C3 site on 01/03/2009.

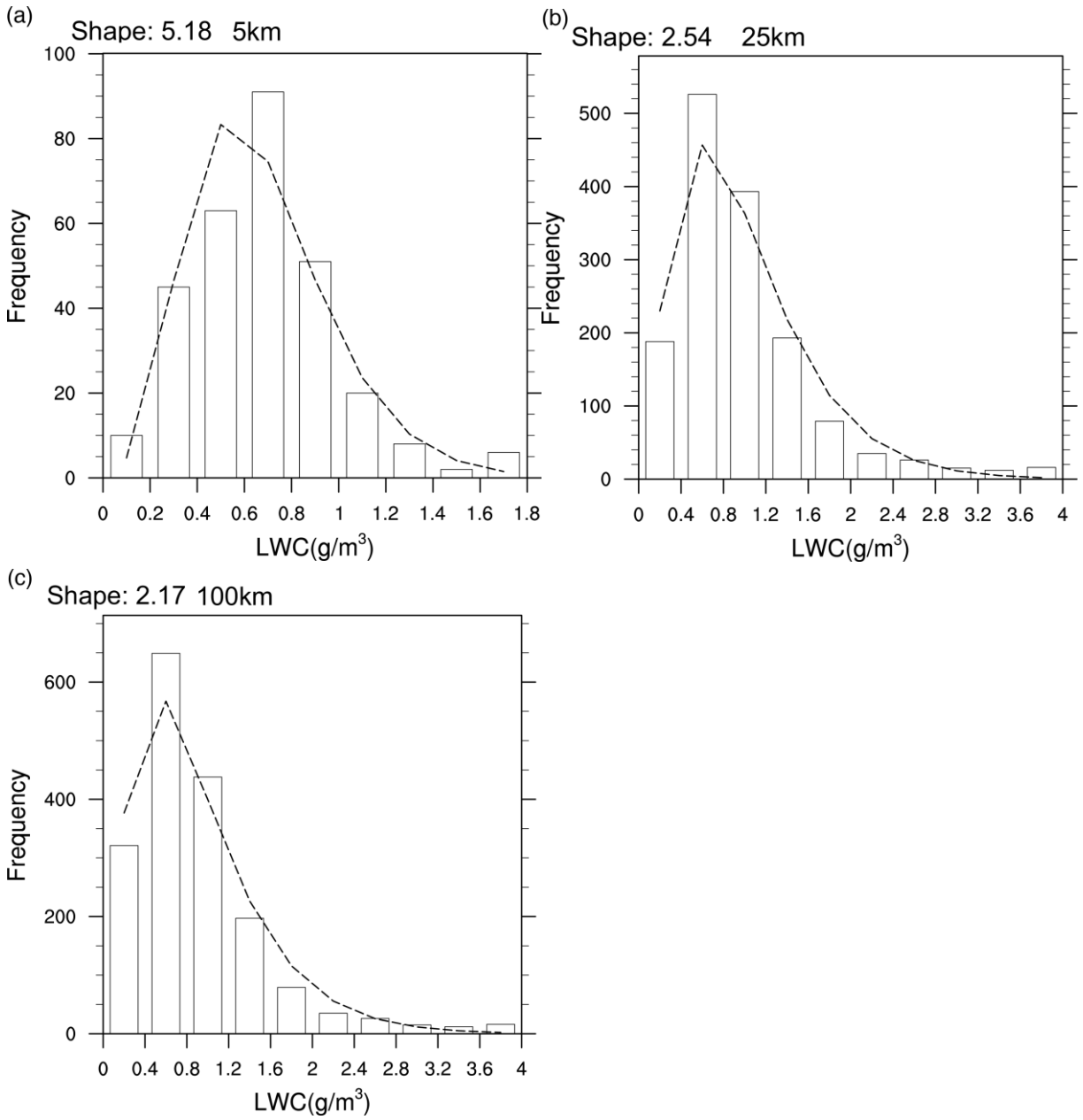

Figure 2.3. Examples of the frequency distribution of cloud water and the Gamma distribution fitting using the maximum likelihood method. The data are from the ARM SGP on 06/03/2009 in Figure 1 at 100 m height. The sampling horizontal scales are 5 km, 25 km, and 100 km for (a), (b), and (c) respectively.

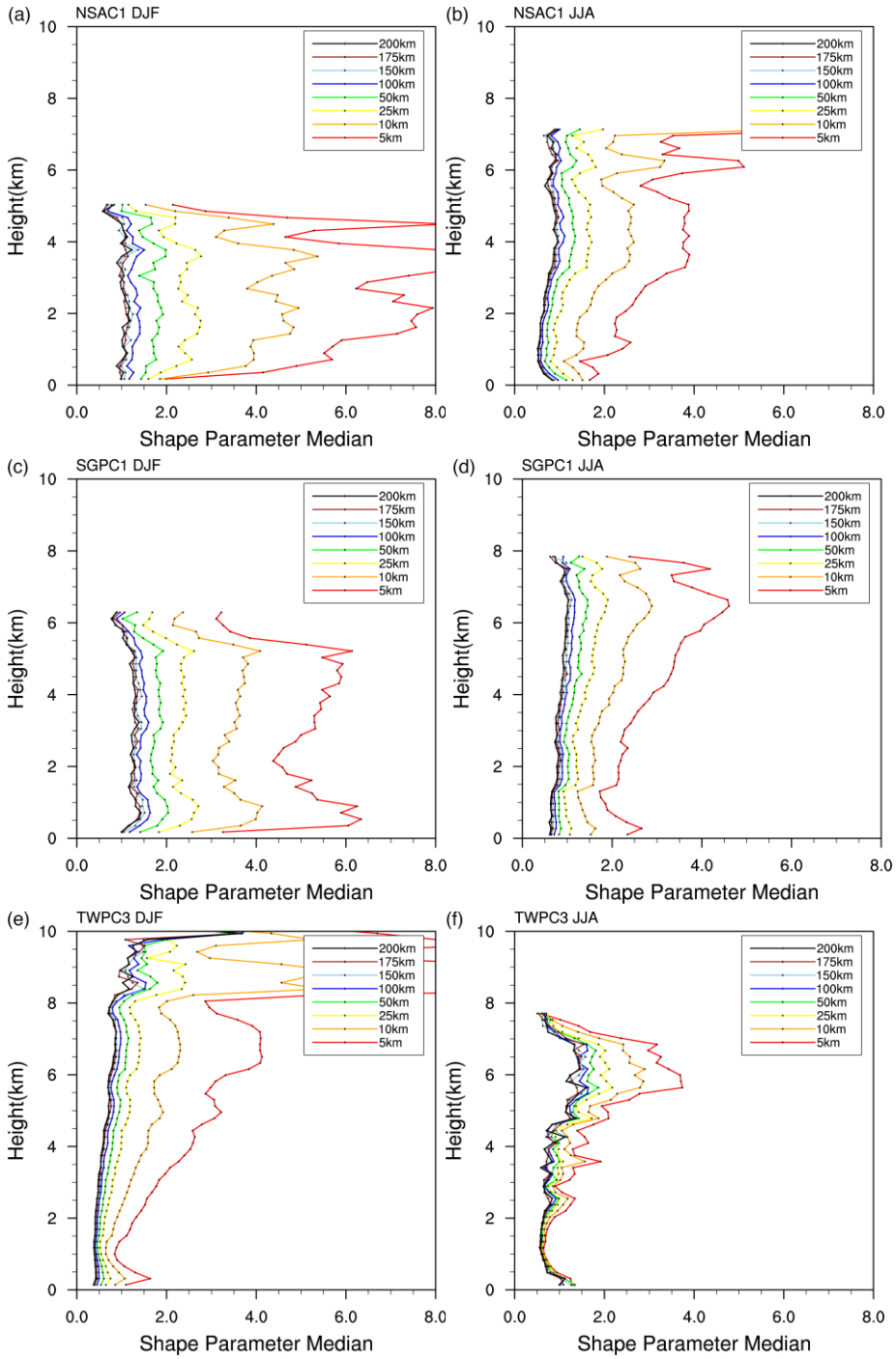

Figure 2.4. The liquid water shape parameter for NSA C1, SGP C1, and TWP C3 sites in DJF and JJA. Different colors represent different scales as shown in the legend.

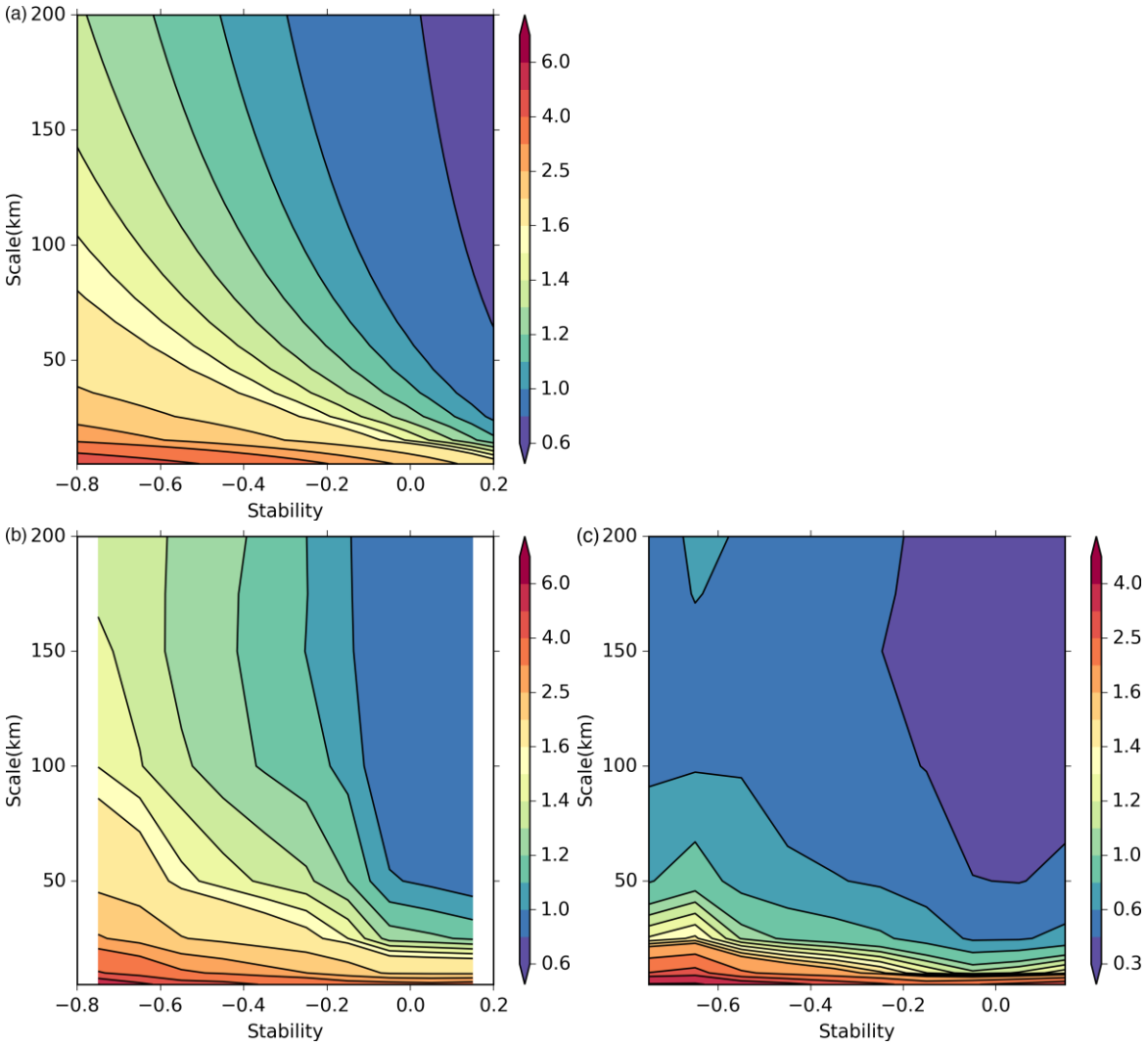

Figure 2.5. (a) The parameterized shape parameter as a function of scale and atmospheric instability. (b) The binned mean of observational shape parameter as a function of scale and atmospheric instability. (c) The binned standard deviation of the random term estimated from observations.

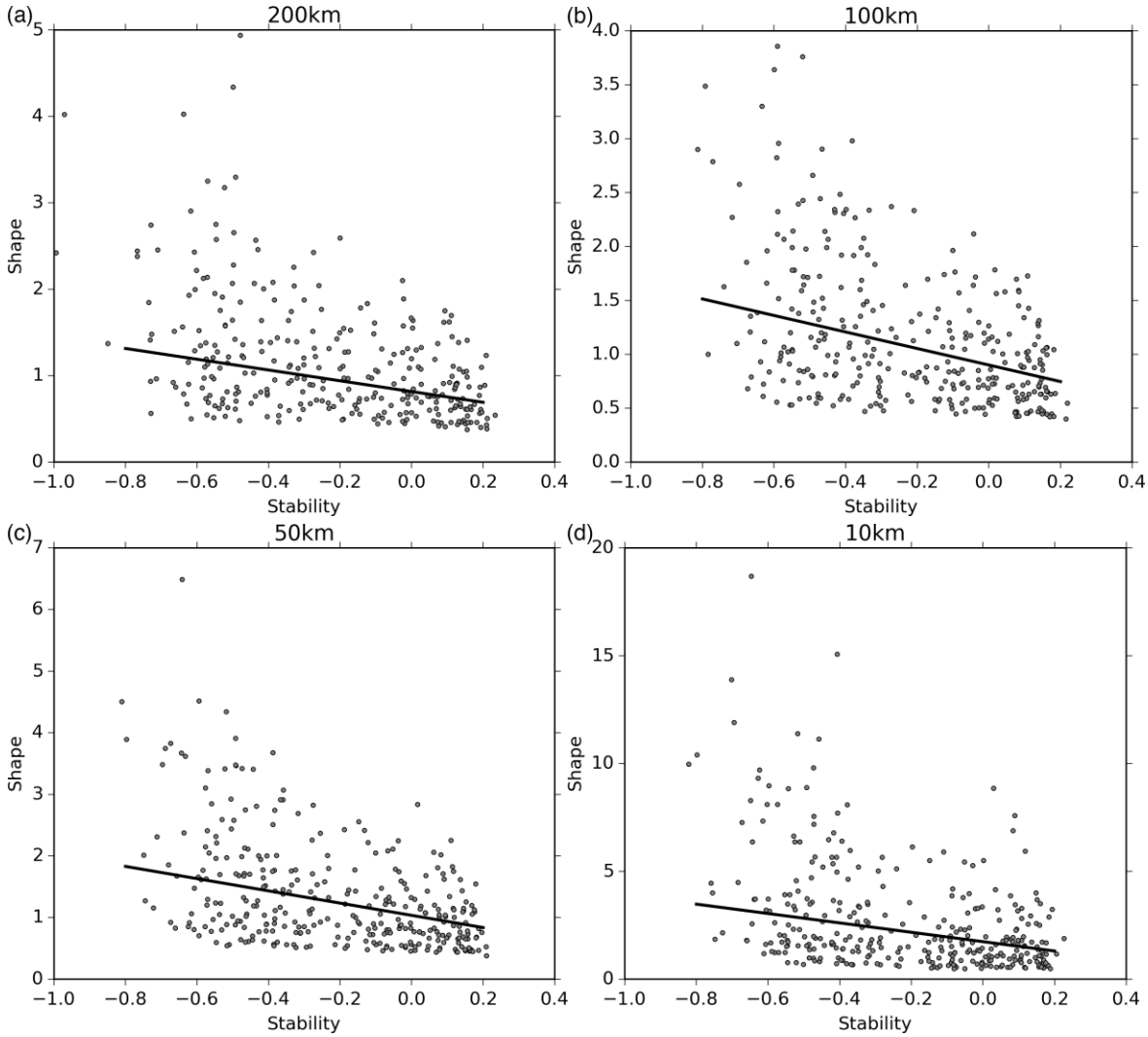

Figure 2.6. Parameterized shape parameter (black solid line) versus observationally derived lower quartile, median, and upper quartile of the shape parameter (gray dots) in each month as a function of atmospheric instability for different horizontal scale: (a) 200 km, (b) 100 km, (c) 50 km, and (d) 10km.

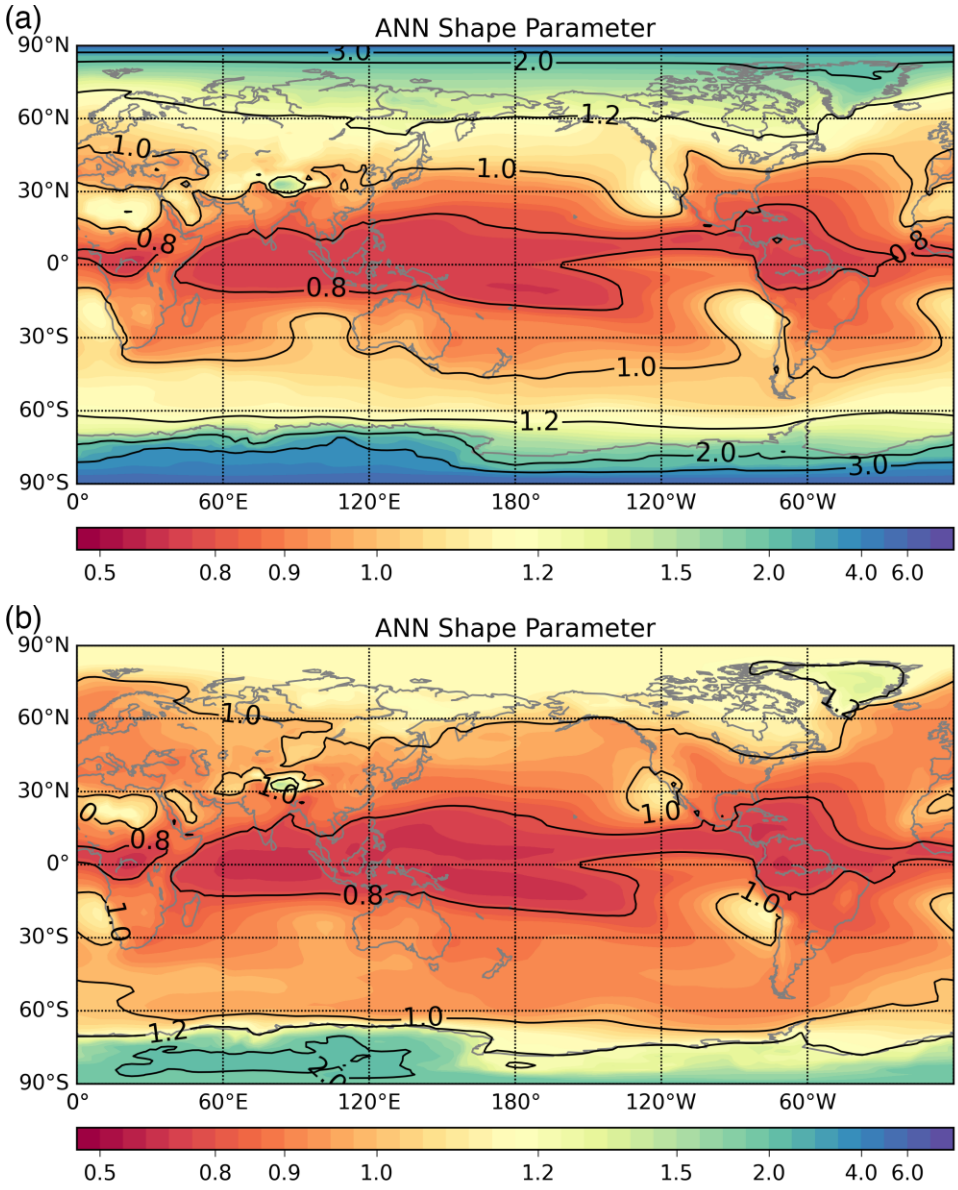

Figure 2.7. (a) Annual mean of global shape parameter distribution diagnosed from CESM simulation using a 2°×2° resolution. (b) same as (a) but assuming global 200 km spatial scale.

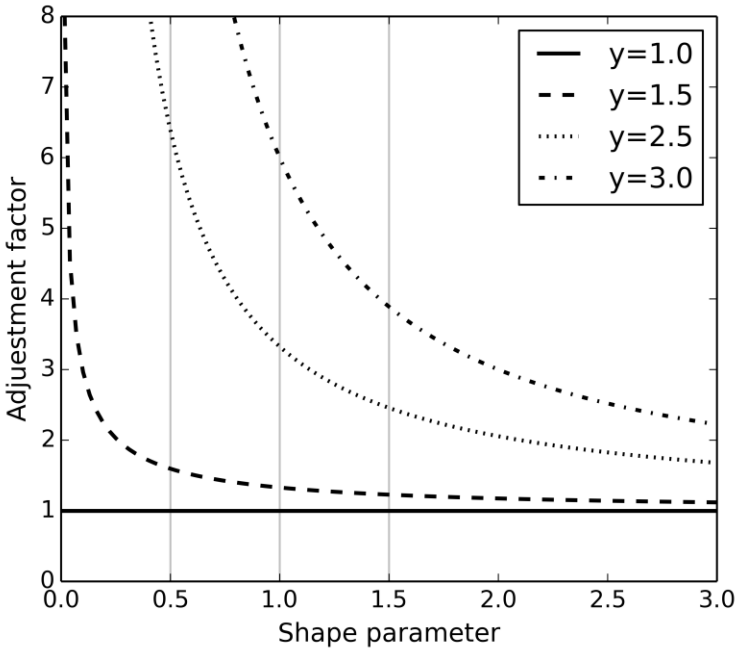

Figure 2.8. The adjustment factor in the conversion rate of microphysics scheme with different power relations (y=1, 1.5, 2.5, 3).

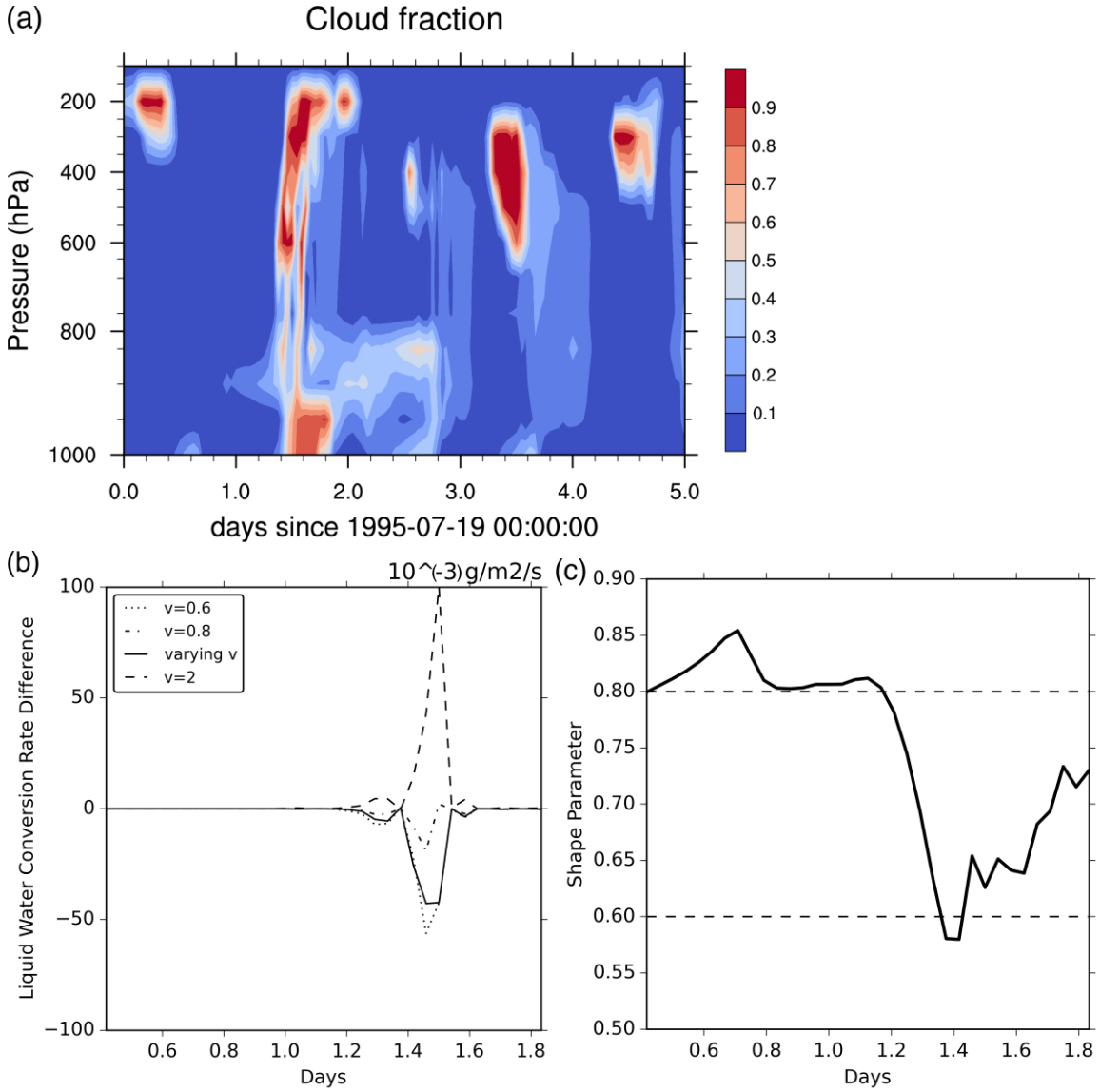

Figure 2.9. (a) Cloud fraction from a 5-day simulation from the single column simulation of CAM5. (b) Column-integrated microphysics liquid water conversion difference by using shape parameter ν=0.6, ν=0.8, ν=2.0 and parameterized varying ν relative to the control simulation of ν=1.0. (c) The corresponding varying ν magnitude.

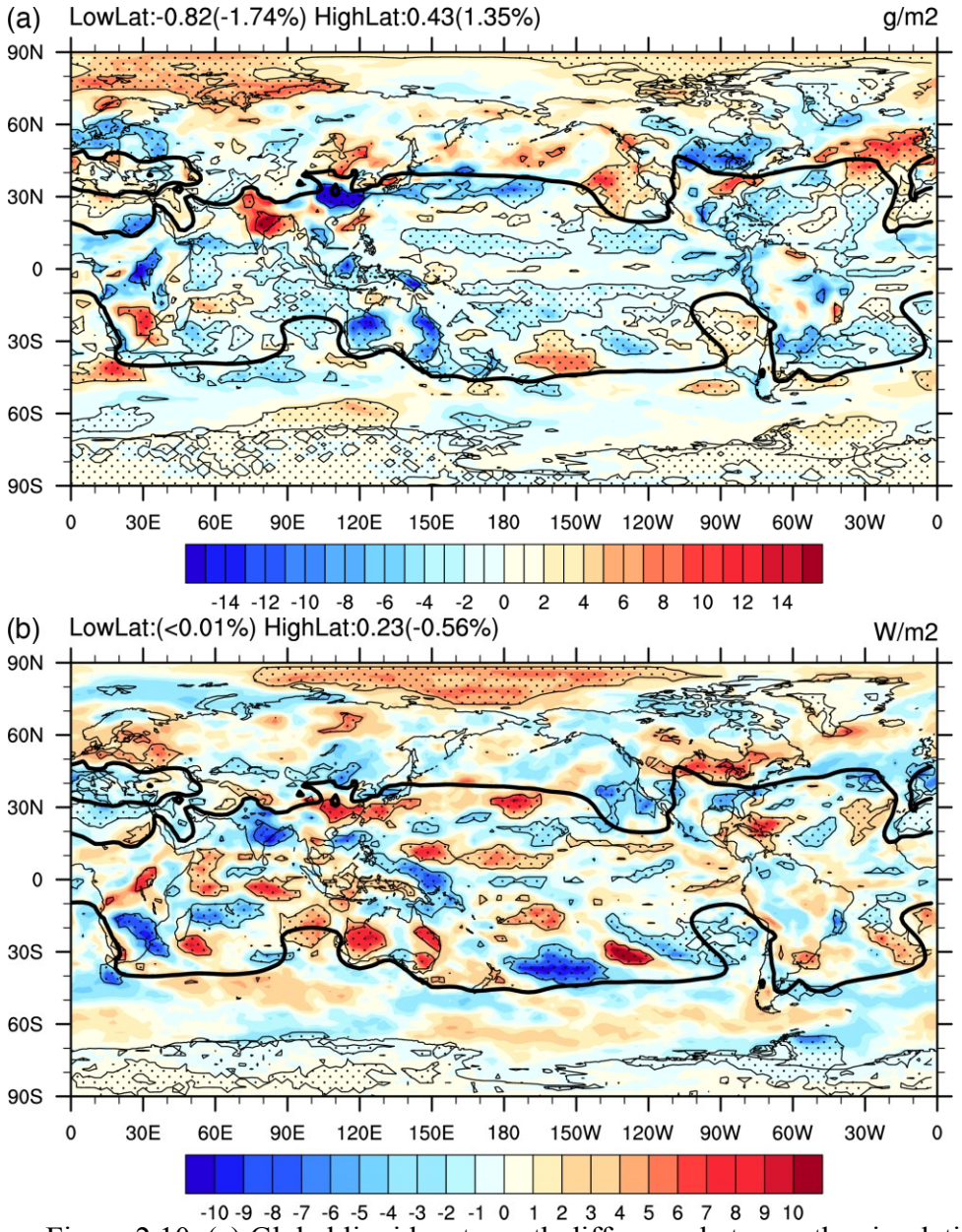

Figure 2.10. (a) Global liquid water path difference between the simulation with varying ν and the control simulation of ν=1.0 (dotted hatch is the area passing the statistical significance test with 95% confidence level). The thick solid line represents the contour of ν=1.0 in the simulation with varying ν. (b) Same as (a) but for shortwave cloud forcing.

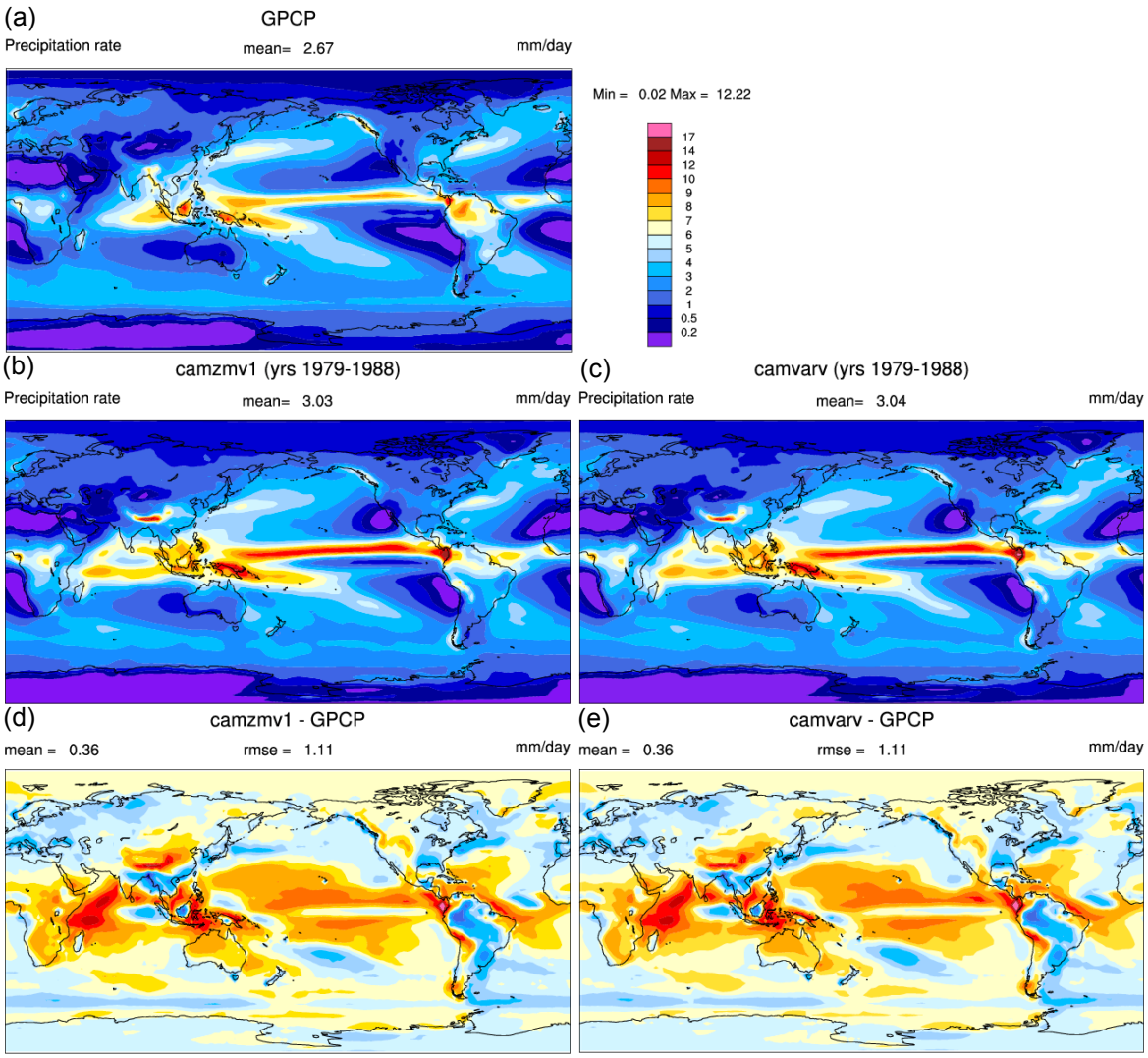

Figure 2.11. Annual total precipitation. (a) observation from GPCP. (b)(d) are the output and the difference from GPCP for the control simulation with fixed $\nu = 1$. (c)(e) are the output and the difference from GPCP for the simulation with scale-aware parameterized ν. The impact of liquid cloud inhomogeneity is very small compared with the control simulation.

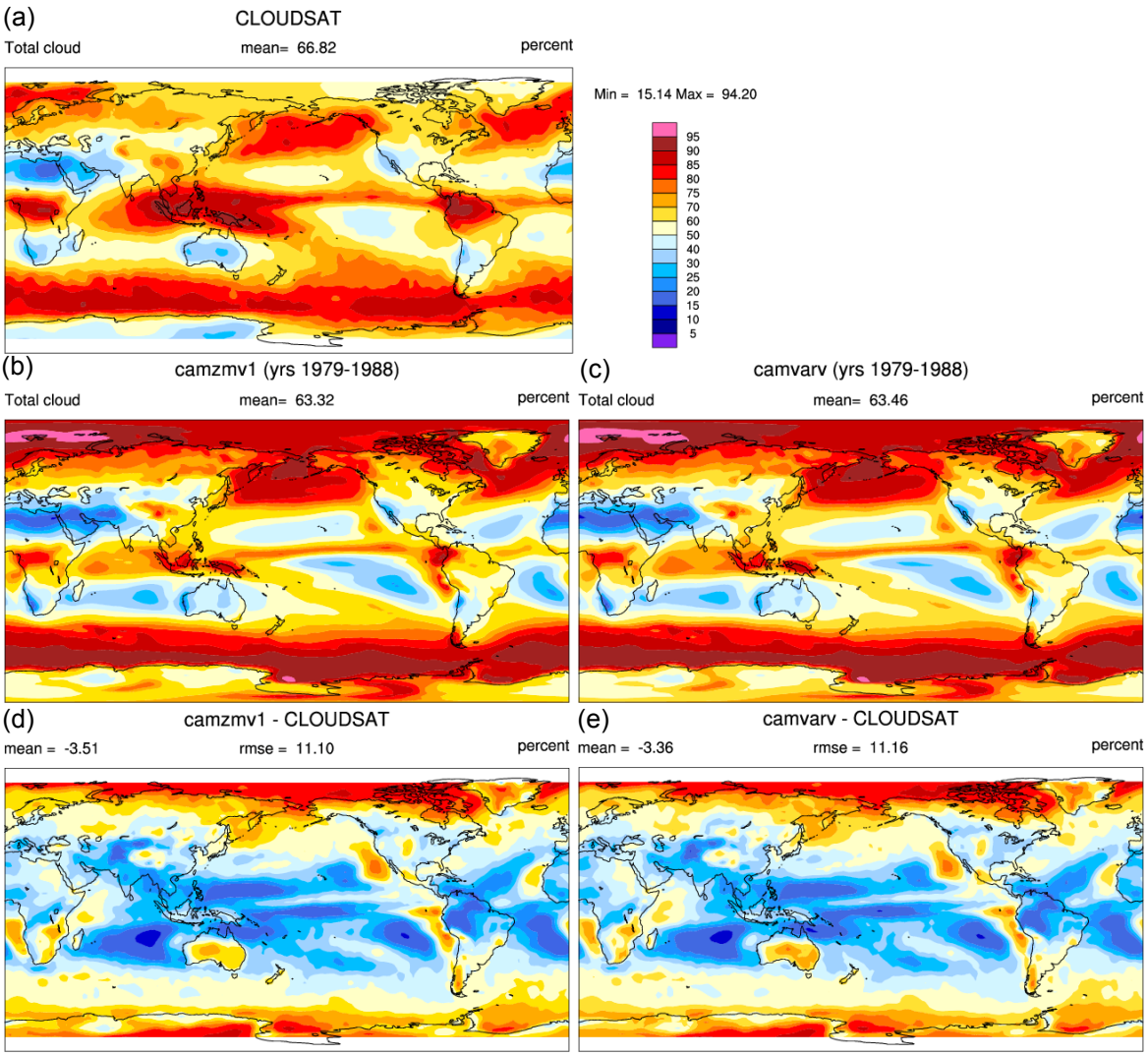

Figure 2.12. Annual total cloud fraction. (a) observation from CLOUDSAT. (b)(d) are the output and the difference from CLOUDSAT for the control simulation with fixed $\nu = 1$. (c)(e) are the output and the difference from CLOUDSAT for the simulation with scale-aware parameterized ν. The impact of liquid cloud inhomogeneity is very small compared with the control simulation.

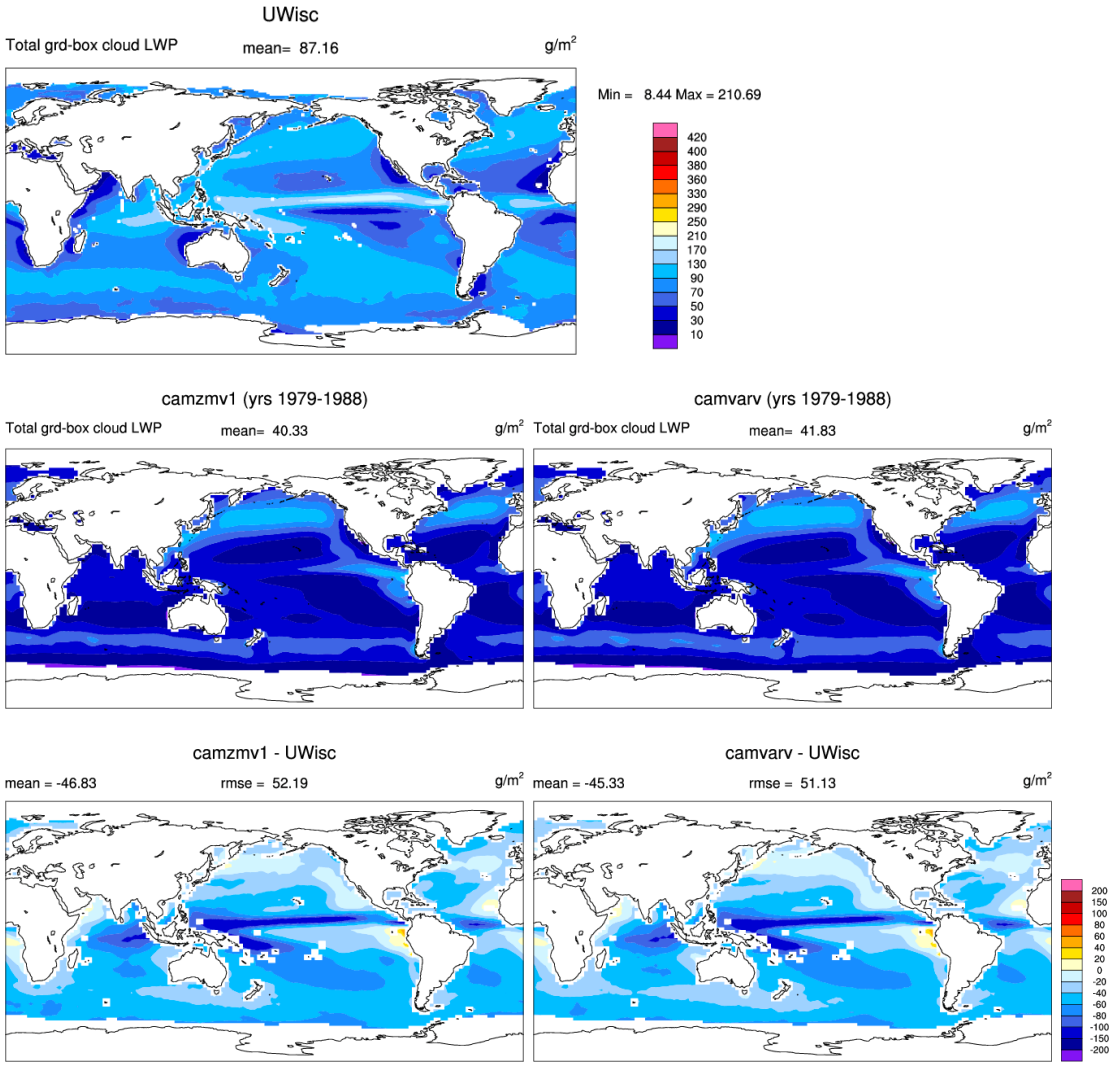

Figure 2.13. Annual total grid-box cloud liquid water path. (a) observation from UWisc. (b)(d) are the output and the difference from UWisc for the control simulation with fixed $\nu = 1$. (c)(e) are the output and the difference from UWisc for the simulation with scale-aware parameterized ν. The negative bias in the control is reduced using varying ν due to the increase of liquid cloud in high latitude.

Chapter 3 Sensitivity of MJO Simulation to Physical Parameters in a Convection Scheme

3.1 Motivation

In the previous chapter, we have discussed the scale dependence of subgrid variability for liquid cloud, its parameterization and its impact on climate simulation. The purpose of all these efforts is to represent the unresolved subgrid-scale processes more accurately in the radiation transfer and microphysics process.

Is it possible to introduce subgrid variability to the convective scheme as we do for microphysics? In fact, this question has been answered back in the 1970s when the early convective parameterization framework was designed. *Yanai et al.* [1973] and *Arakawa and Schubert* [1974] formulated a generalized cumulus parameterization based on convective mass flux that aims to represent the thermodynamic impact of a spectrum of subgrid convective plumes on the large scale environment. A spectrum parameter was chosen to represent a particular cloud type so the final response will be the sum or integration of the ensemble of all subgrid convective clouds, very similar to the idea of what we currently do with microphysics subgrid variability. Many convection parameterizations developed since then have adopted this cumulus parameterization framework.

During the past several decades, great efforts have been made not only to understand and better parametrize convection but also to treat the subgrid variability in more unified and physical way. For instance, *Golaz et al.* [2002] designed a boundary layer cloud scheme that natively adopts a more realistic PDF model that is able to represent not only one or two cloud types but a variety of clouds, such as cumulus, stratocumulus, and clear regimes. *Khairoutdinov and Randall* [2001]

embedded and solved a CRM within a model grid box and let it interact with the large-scale state variables so that a large portion of subgrid cloud process is automatically resolved.

Although great progress has been made to design better cloud parameterization, the simulation performance of most current climate models is far from reality. For example, many climate models suffer from a spurious double intertropical convergence zone (double ITCZ) in the simulated precipitation climatology at eastern Pacific ocean [*Lin*, 2007]. A realistic intraseasonal oscillation or Madden Julian Oscillation (MJO) with correct phase speed and strength still remains a challenge for most models [*Slingo et al.*, 1996; *Waliser et al.*, 2003; *Lin et al.*, 2006].

Several studies have attributed these two biases to the convective parameterization schemes in the models. For example, *Li et al.* [2009] shows that artificially lowering the adiabatic heating profile in a climate model will convert a stationary perturbation in the Indian and west Pacific oceans into a planetary-scale, intraseasonal, and eastward propagating pattern with a phase speed similar to MJO. *Zhang and Song* [2009] found that the moistening of shallow convection may be the key to simulate a realistic MJO when it is working with a revised version of deep convection scheme. *Khairoutdinov et al.* [2005] reported that when superparameterization is used in GCM, not only the double ITCZ bias would be significantly reduced but also the intraseasonal oscillation simulation would be greatly improved.

The latest update or new design of convection schemes have also lead to an improvement of precipitation climatology and intraseasonal variability. For example, in a newly released ECMWF model, a revision of the convection scheme [*Bechtold et al.*, 2008] that adopts an empirical entrainment formulation based on relative humidity led to reduction of both the double ITCZ and MJO biases. *Chikira and Sugiyama* [2010] developed a cumulus parameterization that removes the double ITCZ bias and simulates an east propagating MJO. *Park* [2014] used a unified

convection scheme that allows natural transition from shallow convection to deep convection. It turned out to simulate well both the climatology and MJO.

The key components of a mass-flux based convective parametrization scheme include the cloud model, the cloud properties at the launching level, the entrainment/detrainment calculation, and the closure for cloud base mass flux. What role do each of these components play in changing the MJO simulation? The answer to these questions will provide us a hint about a similar correction that could be applied to the various convection parameterizations in different GCM models.

In this study, we aim to target the MJO bias and determine its sensitivity to several key components in the convection scheme. We will use a relatively simple but flexible multiple-plume convection scheme as our study tool. Each plume is based on a simple mass-flux type bulk cloud model. The scheme is general enough to work as a basis for different types of convection parameterization. In Section 3.2, we present the formulation of this convection scheme. Most of its formulation follows the classical framework by *Yanai et al.* [1973] and *Arakawa and Schubert* [1974] with modifications by *Chikira and Sugiyama* [2010]. In Section3.3 and 3.4, we will introduce the parameter settings in *Chikira and Sugiyama* [2010] and evaluate its standard performance metrics. Section 3.5 will provide sensitivity tests of MJO simulation to several key parameters in the scheme.

3.2 Formulation

The major purpose of convection parameterization is to represent the unresolved subgrid convective impacts on the large-scale environment. Therefore, the final outputs from the scheme are the tendencies of dry static energy (representing temperature change), water vapor, and liquid water. *Yanai et al.* [1973] and *Arakawa and Schubert* [1974] have derived a primitive form of the budget equations representing the tendencies with the contribution from condensation, evaporation,

and vertical heat and moisture transport terms by cumulus plumes. When the convective area relative to the grid size is small and the environmental vertical velocity is only a small fraction of the convective vertical velocity, the tendency equations can be written as follows:

$$
\begin{aligned}
\left(\frac{\partial s}{\partial t}\right)_c &= M_{B,j}\left[L_v\sum_j(C_j - I_j) + L_s\sum_j I_j - L\sum_j EV_j\right] \\
&\quad - M_{B,j}\frac{1}{\rho}\frac{\partial\sum_j\left[m_{u,j}s_{u,j} + m_{d,j}s_{d,j} - \left(m_{u,j} + m_{d,j}\right)s_e\right]}{\partial z} \\
\left(\frac{\partial q_v}{\partial t}\right)_c &= M_{B,j}\left(-\sum_j C_j + \sum_j EV_j - \frac{1}{\rho}\frac{\partial\sum_j\left[m_{u,j}q_{vu,j} + m_{d,j}q_{vd,j} - \left(m_{u,j} + m_{d,j}\right)q_{ve}\right]}{\partial z}\right) \\
\left(\frac{\partial q_l}{\partial t}\right)_c &= M_{B,j}\left(\sum_j C_j - \sum_j I_j - \sum_j R_j - \frac{1}{\rho}\frac{\partial\sum_j\left[m_{u,j}q_{lu,j} + m_{di}q_{ld,j}\right]}{\partial z}\right) \\
\left(\frac{\partial q_i}{\partial t}\right)_c &= M_{B,j}\left(\sum_j I_j - \sum_j S_j - \frac{1}{\rho}\frac{\partial\sum_j\left[m_{u,j}q_{iu,j} + m_{di}q_{id,j}\right]}{\partial z}\right)
\end{aligned}
\tag{3.1}
$$

where the index j represents the contribution from jth plume, q_v is water vapor mixing ratio, q_l is liquid cloud mixing ratio, s is dry static energy $s = c_pT + gz$ (T is temperature), L_v and L_s are latent of vaporation and sublimation, C is the total condensation, I is the part of total condensation freezing into ice, EV is evaporation rate, R is precipitation rate, S is snowing rate, ρ is environmental density, m is the normalized plume mass flux, M_B is the mass flux at the cloud base, the subscript u and d represent the in-cloud properties for updraft and downdraft, and the subscript e represents environmental variables. The C, EV, R, and mass flux terms are all normalized by the mass flux at the cloud base specific to a plume. We assume zero environment liquid and ice condensate ($q_{le=0}$ and $q_{ie} = 0$). Ideally speaking, the more kinds of plume we can include, the more accurate the tendencies terms could be formulated. But the number of plumes has a cost to the computing resources we have. Using too many plumes may not give us a computational advantage over solving a CRM using superparameterization because a CRM not only includes vertical transport but also more internal dynamics of cloud systems. Therefore, we will use as few plumes as possible to meet the design requirement.

To solve for the unknown terms on the RHS of the above equations, we have chosen the classical bulk plume model that has been used in many convection schemes [*Tiedtke*, 1989; *Zhang and McFarlane*, 1995; *Chikira and Sugiyama*, 2010] which assumes horizontally homogeneous in-cloud properties within the individual plumes

$$
\begin{aligned}
E &= em_c \\
D &= dm_c \\
\frac{\partial m_c}{\partial z} &= E - D = (e-d)m_c \\
\frac{\partial h_u}{\partial z} &= e(h_e - h_u) + \frac{L_s \rho I}{m_c} \\
\frac{\partial s_c}{\partial z} &= es_e - es_c + \frac{L_v \rho (C-I)}{m_c} + \frac{L_s \rho I}{m_c} \\
\frac{\partial q_{vc}}{\partial z} &= eq_{ve} - eq_{vc} - \frac{\rho C}{m_c} \\
\frac{\partial q_{lc}}{\partial z} &= -eq_{lc} + \frac{\rho (C-I-R)}{m_c} \\
\frac{\partial q_{ic}}{\partial z} &= -eq_{ic} + \frac{\rho (I-S)}{m_c}
\end{aligned}
\tag{3.2}
$$

where h is moist static energy (MSE) $h = c_p T + gz + L_v q_v$, e and d are fractional entrainment and detrainment rates, the subscript c could be either u or d to represent updraft or downdraft. Other variables are defined the same as in Equation 3.1. We have ignored the plume index j here for simpler notation but this set of equations will be solved for each plume. We only consider the vertical dimension here so it is a set of ordinary differential equations that could be solved upward or downward when the boundary condition, entrainment/detrainment rates e and d, and the relationship among C, I, R, and S can be specified. After solving the cloud model for each plume, the scheme still needs to derive the cloud base mass flux M_B. Additional equation has to be specified to solve M_B, namely the closure. Most mass-flux convection schemes share the above framework and the difference is the way entrainment/detrainment rates and cloud-bass mass flux are calculated.

The following steps describe how the properties of the updraft plume are calculated in our study if the entrainment/detrainment rates e/d are already prescribed:

1. Launching the parcel to cloud base. A launching level is chosen and the boundary conditions of the plume are specified at this level. Typical choices of the launching level are the model surface level or the level with maximum MSE. Larger MSE helps the plume to reach higher level. The initial plume values for h_u, s_u, q_{vu}, q_{lu}, and q_{ic} are usually equal to the environment values at the launching level. Cloud base is usually defined as where the plume begins to become saturated. We may integrate the plume equations for h_u and q_u upward level-by-level. Cloud base is reached when the plume moisture q_u is less than the plume saturated moisture q_{us} (obtained by solving the saturation equation for h_u from *Arakawa and Schubert* [1974]). The updraft mass flux m_u below the cloud base should be solved too but a typical method is to let it decrease to zero from the cloud base to the surface.
2. Launching the parcel to cloud top. After the cloud base is found, the plume properties at this level could be set to what are obtained in the previous step or to a set of newly specified values that include additional turbulent perturbations. In the second circumstance, the cloud properties under the cloud base may have to be solved again using zero condensation C because unsaturation is assumed below the cloud base. At the cloud base, the normalized mass flux m_c has value 1.0 and it is integrated upward using the information of entrainment and detrainment. The MSE h_u could also be solved upward. The plume temperature T_u and water vapor q_{vu} are derived using h_u under the condition of saturation. Because solving h_u may require the prescribed

freezing rate I, we set I to zero first and iterate to let the solution converge. The calculated buoyancy B_u could then be used to determine the cloud top.

3. Microphysics. Above the cloud base the total condensation C is diagnosed from the plume equation of q_{vu}. Once C is solved, the freezing rate I, precipitation rate R, snowing rate S could generally be solved using assumptions of their relationships with C. Precipitation is calculated by integrating the precipitation rate for the whole column.
4. Detrainment at the cloud top. When the cloud top is reached, the plume will decelerate and its mass flux should decrease to zero, which means we must have detrainment rate d larger than entrainment rate e. If the specified entrainment and detrainment do not have such property, we have to enforce the mass flux at top to be zero. The needed detrainment for that could is diagnosed from the mass flux equation. Some convective scheme with vertical velocity information will allow the plume to reach higher than the neutral buoyancy level and this is also used as an option.

Because the framework described above is shared by most mass-flux convection schemes, different choices and the methods to specify entrainment/detrainment rate, the condensation related relationships, and the closure can be tested to investigate the sensitivity of simulation performance to the parameter options. Different combinations of these options lead to a particular version of convective parameterization. For example, when we choose one plume, specify their entrainment/detrainment with moisture convergence and evaporation information, and solve everything else the same, the scheme will work like the *Tiedtke* [1989] scheme.

To evaluate the sensitivity of MJO simulation to various convection options in this study, we have implemented such a plume framework and choose almost the same convection options described in *Chikira and Sugiyama* [2010] with modifications. The reason we choose their

specification is that they have reported an improved MJO simulation with their convection scheme and it would be easier to do sensitivity tests with a scheme that has the possibility of generating realistic MJO. Since previous studies have emphasized the important role of shallow convection, we wish to see if a larger fraction of shallow plumes can enhance MJO. Because their scheme has been only implemented in MIROC4.1, not in other models, we would also like to examine the dependence of the performance of the convection scheme on other models. We will next introduce the method to calculate the entrainment/detrainment rates based on *Chikira and Sugiyama* [2010].

3.3 Plume Specification

A major difference among various convection schemes is how they specify entrainment and detrainment. In the early stage of convection parameterization, entrainment rate of a particular cloud type was considered to depend on cloud size [*Simpson and Wiggert*, 1969] and treated as constant at different heights. *Arakawa and Schubert* [1974] has used entrainment rate as a cloud spectrum parameter, which implies that only one value could be used for a one plume model. However, later observation and CRM modeling studies [*Lin and Arakawa*, 1997] show that entrainment rate could actually depend on height. Therefore, many studies have proposed methods to estimate entrainment rate profile for use in convection scheme. *Gregory* [2001] has proposed a way to estimate entrainment rate by solving a vertical velocity equation using buoyancy information that is more physically based than other empirically determined methods [*Bechtold et al.*, 2008]. His method was used in *Chikira and Sugiyama* [2010] to calculate entrainment rate for different plumes. In this study, we adopt the same formulation. The plume vertical velocity is written

$$\frac{1}{2}\frac{\partial w_u^2}{\partial z} = aB_u - C_\varepsilon aB_u = a(1 - C_\varepsilon)B_u \tag{3.3}$$

where B_u is the plume buoyancy, a and C_ε are tuning parameters with default values 0.15 and 0.5, and w_u is plume vertical velocity. When the initial value at cloud base is given for w_u, we can solve this equation upward. The buoyancy is represented by

$$B_u = g\frac{T_{vu} - T_v}{T_{vu}} \tag{3.4}$$

where $T_{vu} = T_u(1 + 0.61 \cdot q_{vu})$ and $T_v = T_u(1 + 0.61 \cdot q_v)$ are the virtual temperature for plume and environment. The entrainment rate e is then calculated by using the vertical velocity w_u and buoyancy B_u as

$$e = C_\varepsilon \frac{aB_u}{w_u^2} \tag{3.5}$$

For each plume, we assign a particular initial value for w_u. Fourteen plumes with initial w_u ranging from 0.1 m/s to 1.4 m/s are used in *Chikira and Sugiyama* [2010] for cloud base. Each plume will be first lifted from the lowest model level to cloud base (usually the lifting condensation level) and the plume properties at the cloud base will be reset to the environment saturation values at the cloud base. From there, the plume equation and the vertical velocity equation are solved iteratively to the cloud top.

A three-step method is used to solve the equations numerically as described in *Chikira and Sugiyama* [2010]: (1) $B_{u,k-1/2}$ and $w_{u,k-1/2}$ in the lower cloud layer interface are used to estimate the entrainment rate in the middle level e'_k with Equation 3.5. (2) the estimated e'_k is used to solve the estimated plume properties in the upper cloud layer interface $w'_{u,k+1/2}$, $T'_{u,k+1/2}$, $q'_{vu,k+1/2}$, $B'_{u,k+1/2}$, and $e'_{k+1/2}$. The middle level entrainment rate is updated by $e_k = 0.5(e_{u,k-1/2} + e'_{u,k+1/2})$. (3) the updated entrainment rate e_k is used to calculate the final plume properties $w_{u,k+1/2}$, $m_{u,k+1/2}$, $T_{u,k+1/2}$, $q_{vu,k+1/2}$, $B_{u,k+1/2}$, and $e_{u,k+1/2}$ in the upper cloud level interface.

The index $k = 1, \cdots, K$ represents levels from model bottom to top. The mass flux m_u is solved by

$$m_{u,k+1/2} = m_{u,k-1/2} \exp^{(e_k \Delta z)} \tag{3.6}$$

where Δz is the cloud layer depth. The mass flux below the cloud base is given by an exponential function of height z

$$m_u = \left(\frac{z}{z_b}\right)^{1/2} \tag{3.7}$$

where z_b is the height of cloud base. Detrainment is assumed to occur only at the top of the plumes. For a plume equation of a conservative quantity h

$$\frac{\partial h_u}{\partial z} = e(h_e - h_u) \tag{3.8}$$

, we discretize it as

$$\frac{h_{u,k+1/2} - h_{u,k-1/2}}{\Delta z} = e_k \left(h_{e,k} - \frac{h_{u,k-1/2} + h_{u,k+1/2}}{2} \right) \tag{3.9}$$

For cloud microphysics, the total condensation could be diagnosed using a similar discretization of water vapor equation

$$\begin{aligned} &\frac{q_{vu,k+1/2} - q_{vu,k-1/2}}{\Delta z} \\ &= e_k \left(q_{e,k} - \frac{q_{vu,k-1/2} + q_{vu,k+1/2}}{2} \right) + \frac{\rho_k C_k}{0.5 \cdot [m_{u,k-\frac{1}{2}} + m_{u,k+1/2}]} \end{aligned} \tag{3.10}$$

We have assumed that all the source and sink terms of rain (R), cloud ice (I) and snow (S) are related to condensation C through a precipitating fraction F_p and freezing fraction F_i

$$\begin{aligned} R &= (1 - F_p)(1 - F_i)C \\ I &= (1 - F_p)F_i C \\ S &= F_p F_i C \end{aligned} \tag{3.11}$$

The precipitating fraction F_p is given by

$$F_p(z) = 1 - e^{-(z-z_b-z_0)/z_p} \tag{3.12}$$

where z_b is cloud base, z_0 and z_p are 1500 m and 4000 m by default in *Chikira and Sugiyama* [2010]. Their setting is problematic because when $z - z_b < z_0$, F_p is negative, which is not physical. We have set $z_0 = 0$ as default setting. The freezing fraction F_i is given by

$$F_i(T) = \begin{cases} 1 & T \le T_1 \\ (T_2 - T)/(T_2 - T_1) & T_1 < T < T_2 \\ 0 & T \ge T_2 \end{cases} \tag{3.13}$$

where T_1 and T_2 are 258.15K and 273.15K.

Chikira and Sugiyama [2010] also calculated evaporation in the downdraft plumes. Since their impact on MJO simulation has been found to be small, we will not include them in this study. When all the above processes are calculated, the only variable left on the RHS of the budget equation 3.1 is the mass flux at the cloud base $M_{B,j}$ for the *j*the plume. A prognostic cloud kinetic energy equation

$$\frac{\partial K}{\partial t} = AM_B - \frac{K}{\tau_P} \tag{3.14}$$

has been used to provide the closure [*Xu*, 1993]. K is the cloud kinetic energy. A is the cloud work function. τ_P is the dissipation time scale. K can be represented by αM_B^2. α and τ_P are both tuning parameters set to values 5.0×10^7 $kg^{-1}m^4$ and 1.0×10^3s. When M_B is determined, all terms in the budget equations can be derived and the convective precipitation on the surface is calculated from precipitation rate.

With all the tunable parameters set to the default values in *Chikira and Sugiyama* [2010], we replaced both the shallow convection scheme and deep convection scheme in CESM version 1.2.1 and we call it the control version. In Section 3.4, we will evaluate its standard climatology and

MJO performance in the single column model and GCM, and compare its simulation with that of CESM default setting. In Section 3.5, we will use different options in the scheme and analyze the sensitivity of MJO simulation to these parameters.

3.4 Results with Default Parameter Settings

Since the convective parameterization described above is a multiple plume scheme, it would be interesting to see how the in-cloud property of each plume changes with height. Similar to *Chikira and Sugiyama* [2010] (hereafter CS), we have chosen an atmospheric profile that is easy to trigger convection. The profile is the averaged profile in the Tropical Ocean Global Atmosphere Coupled Ocean-Atmosphere Response Experiment (TOGA-COARE) with precipitation larger than 20 mm day^{-1} for 10 November-10 December, 18 December-23 January, and 31 January-18 February. Figure 3.1 shows the in-cloud properties calculated by the plume equation with vertical velocity ranging from 0.1 m/s to 1.4 m/s spaced at intervals of 0.1 m/s. We note large variability among the plumes. A plume with larger initial vertical velocity tends to reach a higher level up to about 8 km, because its entrainment rate is smaller. A tall plume has larger overall vertical velocity, buoyancy, and mass flux. Plumes with smaller initial vertical velocity has larger entrainment rate they would lose their buoyancy within a few kilometers. These plumes represent shallow convection. Since there are no detrainment terms specified in the plume equation, the mass flux of each plume increases monotonically until it reaches the cloud top. The sum of mass flux over all plumes produces a gradual decrease (the blue line in (e)) due to the sharp detrainment of each plume at the top.

Compared with the results given by the Figure 1 of CS, even with all the same parameters and options, our version seems to produce in-cloud MSE closer to the environment saturated values.

The reason could be due to the difference in implementation detail but the overall pattern looks reasonable.

We have set all parameters the same as in CS and name it DEFAULT. We first conducted a single column simulation with observational forcing from the TOGA-COARE case starting from 12/19/1992 for twelve days. We have run the same case using the standard CESM version 1.2.1 with both ZM deep convection [*Zhang and McFarlane*, 1995] and UW shallow convection [*Park and Bretherton*, 2009] for comparison (hereafter CAM).

Figure 3.2 shows the simulated precipitation during the twelve-day TOGA-COARE period from CAM and DEFAULT. The observation shows several large precipitation peaks transitioning gradually into a period of less precipitation activity after day 7. CAM is able to capture this smooth pattern very well. The phase of CAM convective precipitation seems to be delayed for a few hours from observation. To the contrary, DEFAULT shows a very different sporadic precipitation with extremely large peaks. Almost all the precipitation is from the convection scheme. Figure 3.3 displays the heating rate contributed by convection scheme for CAM and DEFAULT, compared with the observational Q1. CAM produces very smooth heating pattern consistent with the observation even though the heating height is lower than that observed, especially from day 2 to day 3. DEFAULT simulated very irregular and sharp heating features corresponding to its precipitation pattern. The convection heating is in the lower troposphere, implying that a greater of shallow convection is involved. Figure 3.4 shows the corresponding moisture tendencies. These moistening patterns for both versions are consistent with their heating patterns. CAM produces a drying pattern below its heating center while moistening at the top by detrainment. We see that DEFAULT is creating too much heating that stabilizes the atmosphere too quickly so that it is not able to trigger convection continuously. The all-time average of the heating profile in Figure 3.5

shows that DEFAULT heating rate is about two times that observed in CAM. Both CAM and DEFAULT generate lower heating rate centers than observed.

From the results of the single column run, we can see that a default set of parameters that work well in a model may not be a suitable configuration for another. The process that controls the convective strength in DEFAULT is the prognostic closure Equation 3.14. The dissipation time scale τ_p and tunable parameter α in DEFAULT may not work with CESM and may need to be re-tuned.

Next, we briefly show a few examples of the GCM climatology and variability with these default settings. The GCM simulation is set up as a AMIP-type 5-year simulation forced by climatological sea surface temperature (SST). Figure 3.6 shows the annual mean precipitation by CAM and DEFAULT. CAM produces a generally reasonable global precipitation distribution but it suffers from a positive double ITCZ bias at east Pacific Ocean. DEFAULT does not have such bias, consistent with the results by CS, while biases from other regions increase dramatically, such as too much precipitation in western Pacific warm pool and Indian Ocean, too little precipitation over the Amazon and Africa, and too much extension of southern ITCZ. Figure 3.7 shows the simulated MJO east-westward and north-southward propagating pattern in the tropics from observation, CAM and DEFAULT. Neither CAM nor DEFAULT are able to reproduce the strong and sustained eastward OLR propagating signal (shading) and the coupled 850mb zonal wind (shown in contour) from the reference point in the Indian ocean. There is a very weak propagation of zonal wind toward the east in CAM and DEFAULT but its phase speed is too fast. The power spectra plot in Figure 3.8 also reveals these deficiencies of the models. The peak around the frequency with period 45 days and wave number 1 in the observation is not captured in both models. Again, the default parameter settings used by CS is not directly transferable to CESM, so the good

MJO performance reported in CS scheme is not observed. In the following section, we will use several options to investigate the roles of some of the key parameters in changing the MJO simulations.

3.5 Sensitivity Test

As mentioned at the beginning of the chapter, many previous studies have emphasized the important role of shallow convection in enhancing MJO by preconditioning the atmospheric moist environment in the low troposphere. We designed two experiments to control the relative population of deep and shallow plumes to investigate the sensitivity of MJO simulations.

The key parameters to determine the height of convective cloud top are the choice of launching level, initial plume vertical velocity, and entrainment rate. In the offline calculation, DEFAULT version generally exhibits lower plumes than that in CS with the initial vertical velocity ranging from 0.1 m/s to 1.4 m/s. We discovered that an enlarged range from 0.2 m/s to 4 m/s with 15 plumes will help the plumes reach a higher level, similar to that shown in CS Figure 3.9. With this change, the plumes generally reach a higher top with larger buoyancy and have slightly higher mass flux centers. These plumes could be considered as deep plumes (hereafter DP).

For the shallow plumes, we seek smaller vertical velocity and larger entrainment rate so that the plumes lose buoyancy faster. We slightly reduce the vertical velocity range to 0.1 m/s-1.2 m/s and increase the plume entrainment rate by changing the parameter C_ε to 0.8. From Equation (3.3) and (3.5), we know that the increase of C_ε will lead to larger entrainment rate. The launching level in CS is the LCL and all the plume variables are reset to the environment saturated values. Therefore, the cloud base could be several model levels higher than the surface. We have changed it to launch from the maximum MSE level and then reset the plume properties to the environment saturated values. We show the offline calculation with all these modifications in Figure 3.9 and

Figure 3.10. We can see that the modifications indeed led to deep (hereafter DP, Figure 3.9) and shallow plumes (hereafter SH, Figure 3.10).

We found that the strong and sporadic heating and precipitation problem in DEFAULT can be largely alleviated by changing the parameters α and τ_p in the closure equation. Larger values of α and τ_p slower the converting rate of cloud work function into cloud base mass flux and dissipation rate according to Equation 3.14. The sharp pattern in heating profile and precipitation could be reduced by such modifications. We have used the values 5×10^{11} and 2×10^{7} for α and τ_p in shallow plumes and the values 4×10^{10} and 8×10^{5} for α and τ_p in deep plumes. We have repeated the single column simulation for the TOGA-COARE case using both DP and SH shown in Figure 3.11 and Figure 3.12 respectively. It is seen that in both of these cases, precipitation patterns are much better than DEFAULT. They follow the observations well. SH is able to capture the precipitation phase well while DP precipitation peak is usually delayed for a few hours. Generally speaking, the heating center of DP is always higher and that of SH is lower.

To test which type of plumes are more favorable for MJO, we did the same GCM simulation using SH and DP as we did for DEFAULT and plot the lag regression map in Figure 3.13. SH reproduces both the eastward and northward MJO propagation pattern very well as shown in Figure 3.13(b). Not only is the OLR propagating signal strong but it is well coupled with the 800mb zonal wind structure with a reasonable phase speed, similar to observation. On the contrary, DP produces very noisy and localized pattern in the lag regression plot, implying no MJO propagating signal at all. A further examination in Figure 3.13 shows that SH may have a slightly smaller frequency than that in observation. With only several modifications of the convective parameters, we are able to generate totally different MJO patterns. The simulation of MJO is sensitive to the choice of launching level, entrainment rate specification, initial vertical velocity, and the

dissipation time scale in the closure. Shallower convection with lower and broader heating rate tends to enhance the MJO propagating. *Li et al.* [2009] found that an artificially lowered heating rate helps to improve MJO simulation. Our results are consistent with their conclusion but the heating is naturally applied by multiple plumes.

Since there are several differences between DP and SH, it would be useful to know which one or two components are more important than the others. We have tried to apply the combination of the modifications one at a time to see which contributes most to improvement of MJO simulation. Figure 3.14 shows the MJO lag regression plot with several combinations we have tried. We can see from all the figures that making any one single modification cannot not produce the good MJO as SH does. The most significant improvement comes from simultaneously applying both initial vertical velocity range and entrainment rate changes (see (d)). Note that the launching level used by SH has been applied to all test cases. A removal of this modification will result in noisy and localized MJO signals.

Note that in the shallow setting for convection plumes, parameters are adjusted to allow more shallow convection to take place but it does not imply that deep convection is never triggered. The overall enlarged entrainment rate for the shallow setting dilutes the lifting plumes more efficiently and most plumes reach their neutral buoyancy level at lower heights. But when the environment profile is favorable for the deep convection, more plumes are able to reach higher. This could also be seen in Figure 3.11 that the weak heating range could still expand up to 200mb, only slightly lower than that for the deep plume setting. Therefore, deep convection still plays a role under shallow plumes but its fraction is less. This is also the advantage of using multiple plumes, representing both shallow and deep plumes in a unified way.

3.6 General GCM Performance

Besides the MJO sensitivity test, we provide a general GCM simulation test for the version with shallow plumes. The simulation setting is a 5-year AMIP run the same as the previous run. Figure 3.15 shows the map of climatology precipitable water and total precipitation. The global mean precipitable water is slightly larger than the observation, implying a more moisture atmosphere using SH. The precipitation shown in Figure 3.15 (b) is better than that simulated by DEFAULT in Figure 3.6. No double-ITCZ bias is observed. The land precipitation over Amazon and Africa is close to the observation. However, the overall precipitation magnitude is too large compared with the observation. There is also a large positive bias in the Indian Ocean. The convection strength may need to be further tuned down by adjusting the time scale parameters in the closure to remove such biases.

Figure 3.16 shows the cloud distribution simulated in low, middle, and high levels. There is too much low cloud simulated by SH while lacking moderate amount of middle and high cloud compared with the observation. These biases introduce the radiation unbalance at TOA shown in Figure 3.17. Too much low cloud reflects larger amount of shortwave radiation, producing an 8 w/m^2 bias compared with observation while the upward longwave radiation shown in (b) is close to the one simulated by the CAM default setting (not shown). This could indicate too much shallow convection in the shallow-plume settings. The fraction of shallow plumes could be slightly reduced to provide a better low cloud distribution while keeping a reasonable MJO propagation.

Figure 3.18 shows the diurnal cycle simulated by both SH and CAM default version, compared with the observation. The precipitation peak over the tropical ocean in CAM default version is in the local early morning, earlier than observational late morning. SH is able to represent the observational diurnal cycle over the ocean well. However, the observational late afternoon and

evening precipitation peak over land is not captured by both SH and CAM default version. There is a late afternoon feature over North America with SH but the strength is too weak.

In summary for the general GCM performance, SH simulates a better Pacific precipitation distribution and diurnal cycle but the other fields such as radiation and low cloud distribution deteriorate. Since SH is a version targeted for MJO sensitivity study, the convection parameters and the parameters in other cloud schemes have not been tuned sufficiently. Future work may be required to adjust the model parameters for an overall better simulation of both climatology and intraseasonal variability.

3.7 Conclusion

In this study, we have used a multi-plume convection parameterization to study the MJO sensitivity on convective configurations and parameters. This parameterization was implemented to be flexible enough so that different convection configurations such as entrainment/detrainment rates, plume designation, launching level, and microphysics, can be tested.

When the *Chikira and Sugiyama* [2010] scheme is directly used in CAM, we found that the default parameters are not compatible with CAM. After making several modifications to the scheme, we are able to reproduce a very strong MJO propagation using an option of enhanced shallow convection. The key components of the successful MJO simulation consist of launching the plumes from the level of maximum MSE, larger entrainment rate, and weaker initial vertical velocity range for the launching plumes.

This sensitivity study is a first step toward a better understanding of MJO simulation. The set of parameters for shallow plumes have been found to favor MJO propagation but we haven't been able to validate them with the realistic values, which requires extensive observation. However, a benefit of using multiple plume convection scheme is that the distribution of plume in-cloud

properties is given. The plume properties solved by the cloud model can be compared with and constrained by the results from cloud resolving models or observations. Moreover, the specification of entrainment/detrainment rate and plume properties from the other convective scheme or experimental design could be used as options. Ensembles with different options can be also tested. Within the parameterization framework and implementation presented, new parameterization ideas can be tested and evaluated.

Figures

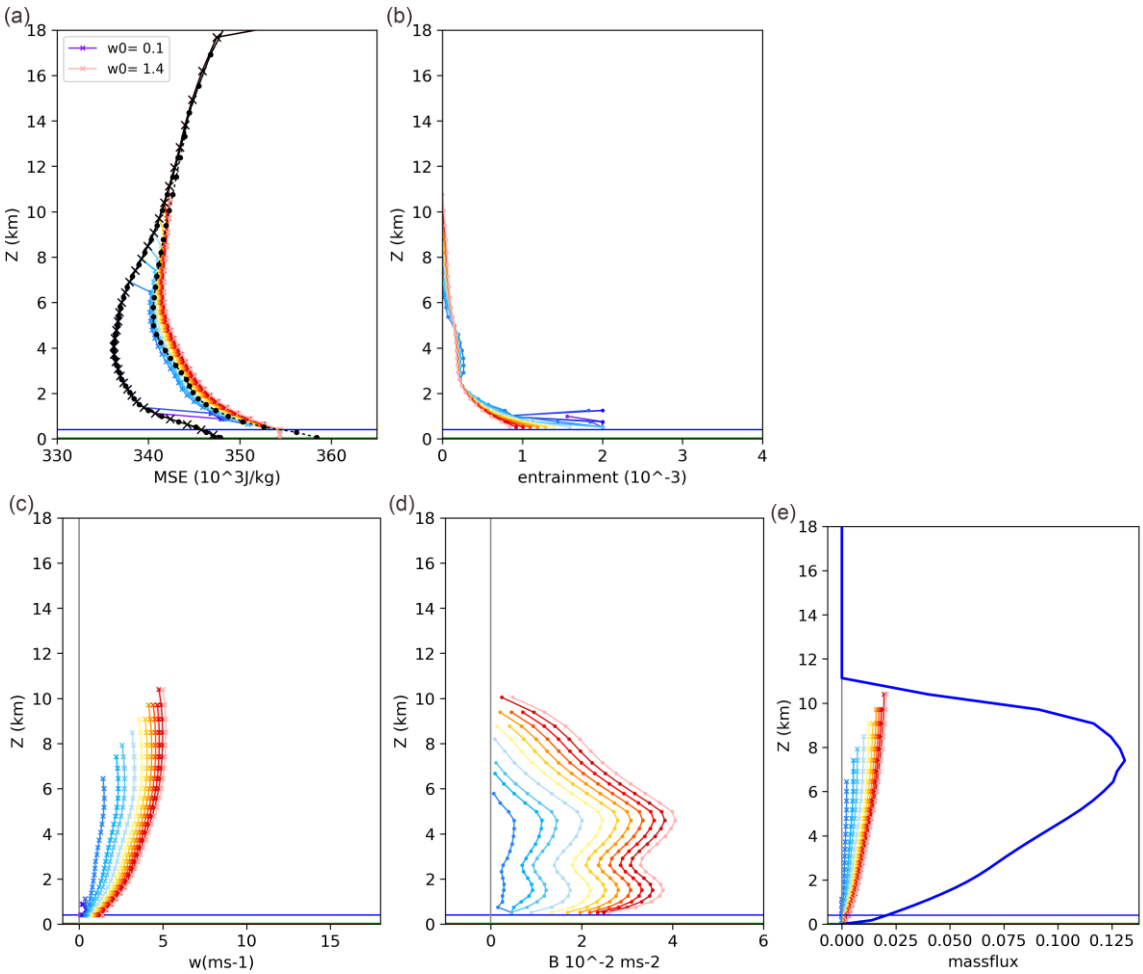

Figure 3.1. Offline calculation with an average profile from TOGA-COARE. Different colors represents plumes with initial vertical velocoties from 0.1 m/s to 1.4 m/s. (a) Plume MSE (lines in colors), environemtn MSE (solid black line), enviroment saturated MSE (dash line). (b) Entrainment. (c) vertical velocity. (d) Buoyancy. (e) Normalized mass flux (blue line represents the sum of mass flux of all plumes). Dot and cross marks represent properties present in the middle of model level and on the interface respectively.

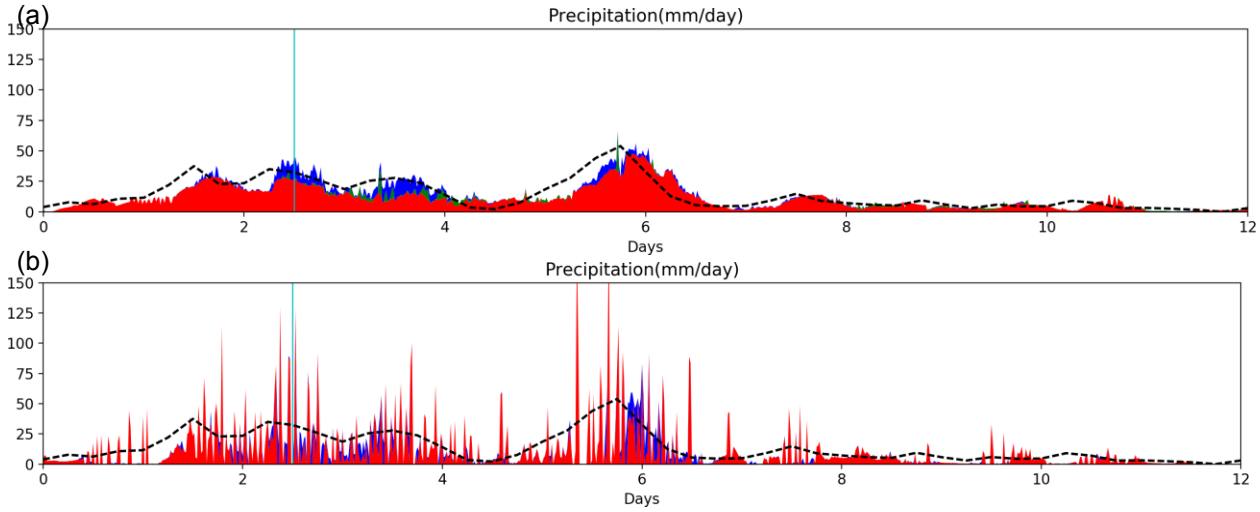

Figure 3.2. Precipitation (mm/day) simulated in the TOGA-COARE single column run. The black dash line is the observation from TOGA-COARE. (a) and (b) are respectively for CESM default ZM+UW setting and the current convection scheme with the default parameters. All precipitation amount is additive from the components: large-scale precipitation(blue), shallow precipitation (green), and the convective precipitation(red). The precipitation from DEFAULT convection is all considered as deep but it may have shallow components in it.

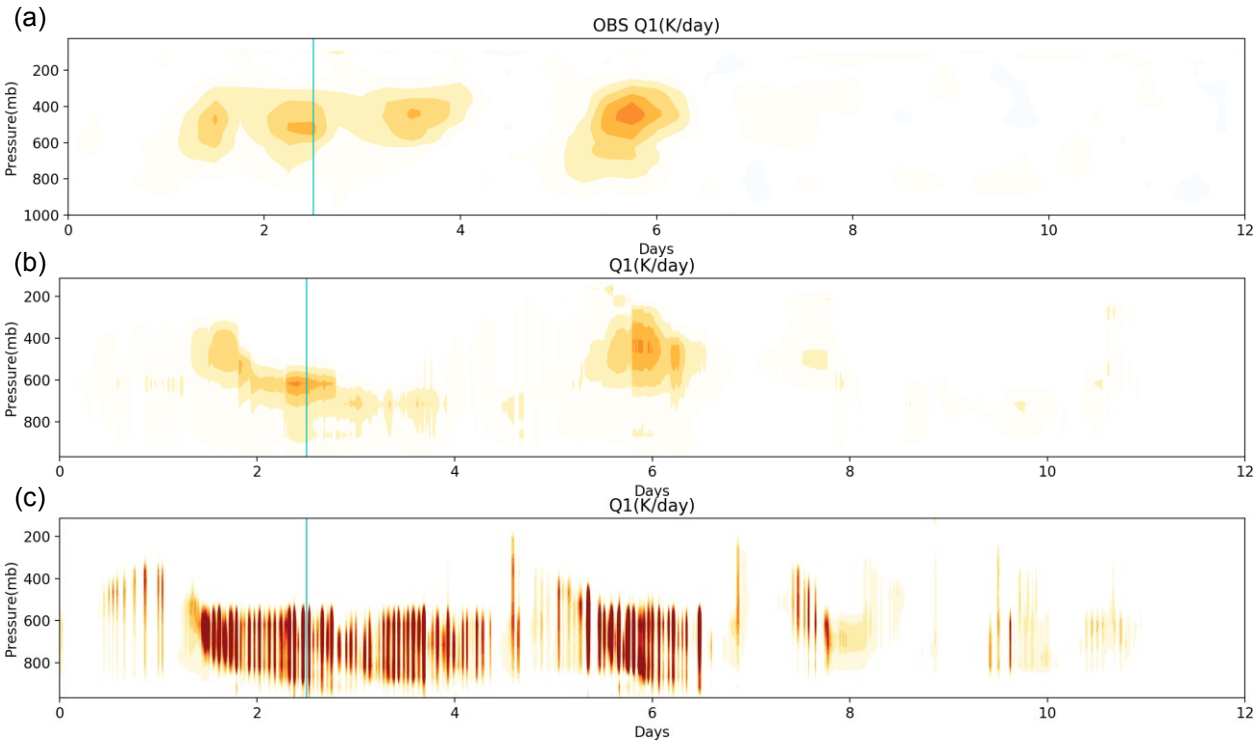

Figure 3.3. Heating rate contribution only from the convection scheme simulated in the TOGA-COARE single column run. (a) is the observational heating rate from TOGA-COARE including all physical terms. (b) and (c) are for CESM default ZM+UW setting and the current convection scheme with the default parameters.

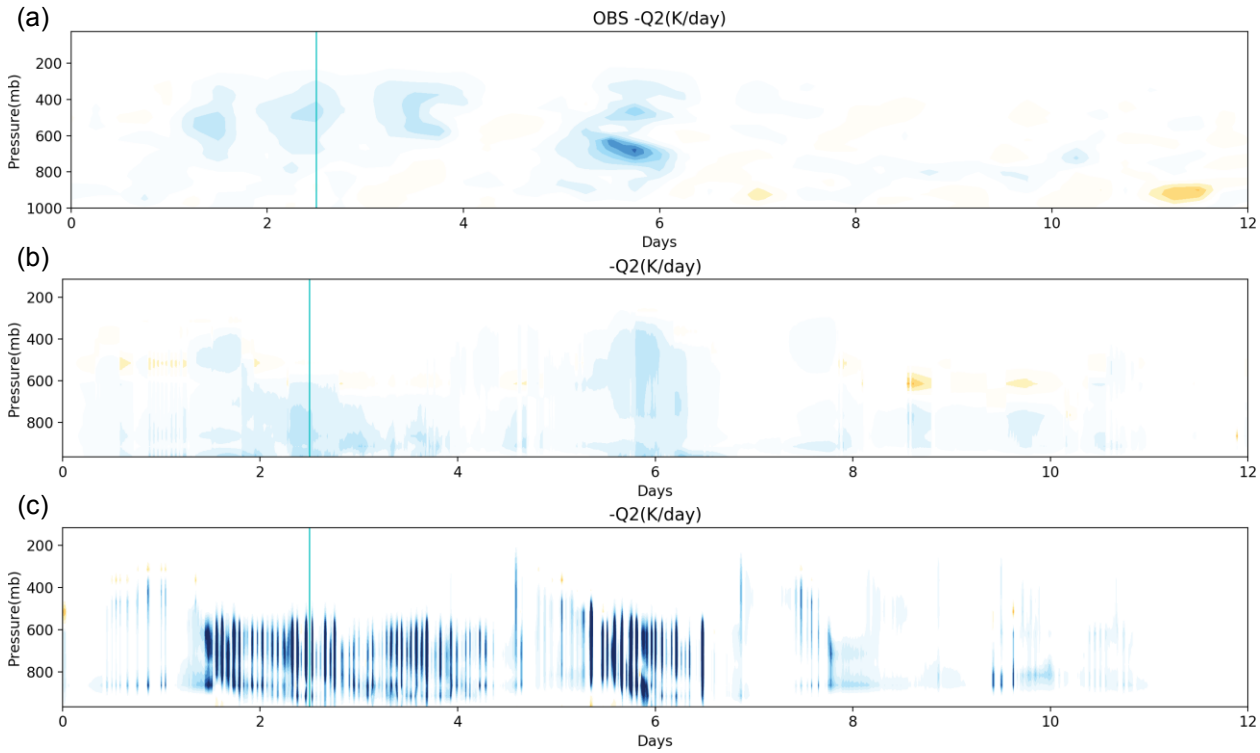

Figure 3.4. Moisture tendency contribution only from the convection scheme simulated in the TOGA-COARE single column run (unit converted into K/day). (a) is the observational moisture tendency from TOGA-COARE including all physical terms. (b) and (c) are for CESM default ZM+UW setting and the current convection scheme with the default parameters.

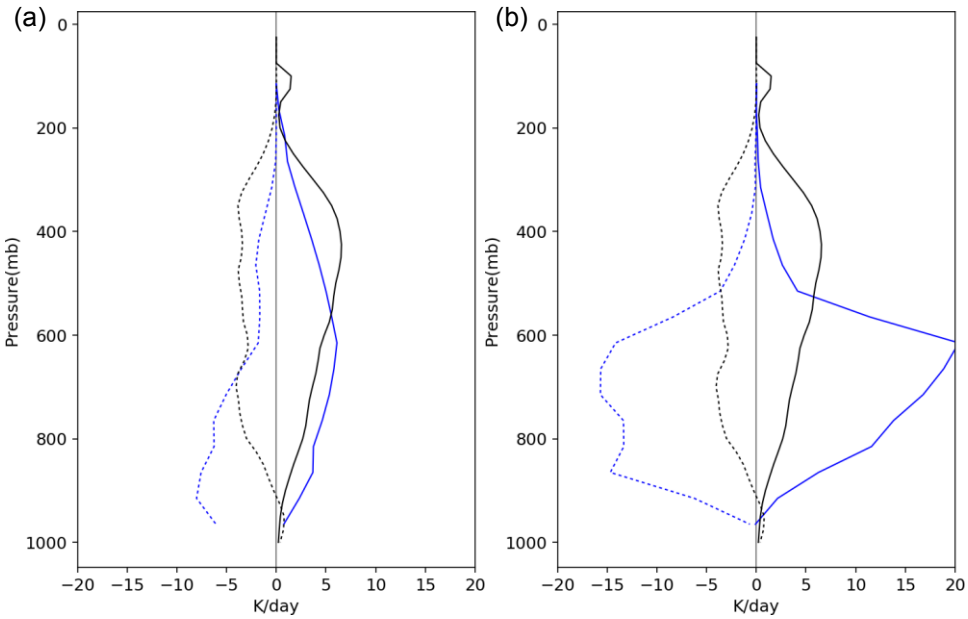

Figure 3.5. All-time averaged heating (solid line) and moisture (dash line) tendency contribution only from the convection scheme simulated in the TOGA-COARE single column run (unit converted into K/day). Observations are shown in black and simulation are shown in blue. (a) is the output from the CESM default ZM+UW setting. (b) is the output from the current convection scheme with the default parameters.

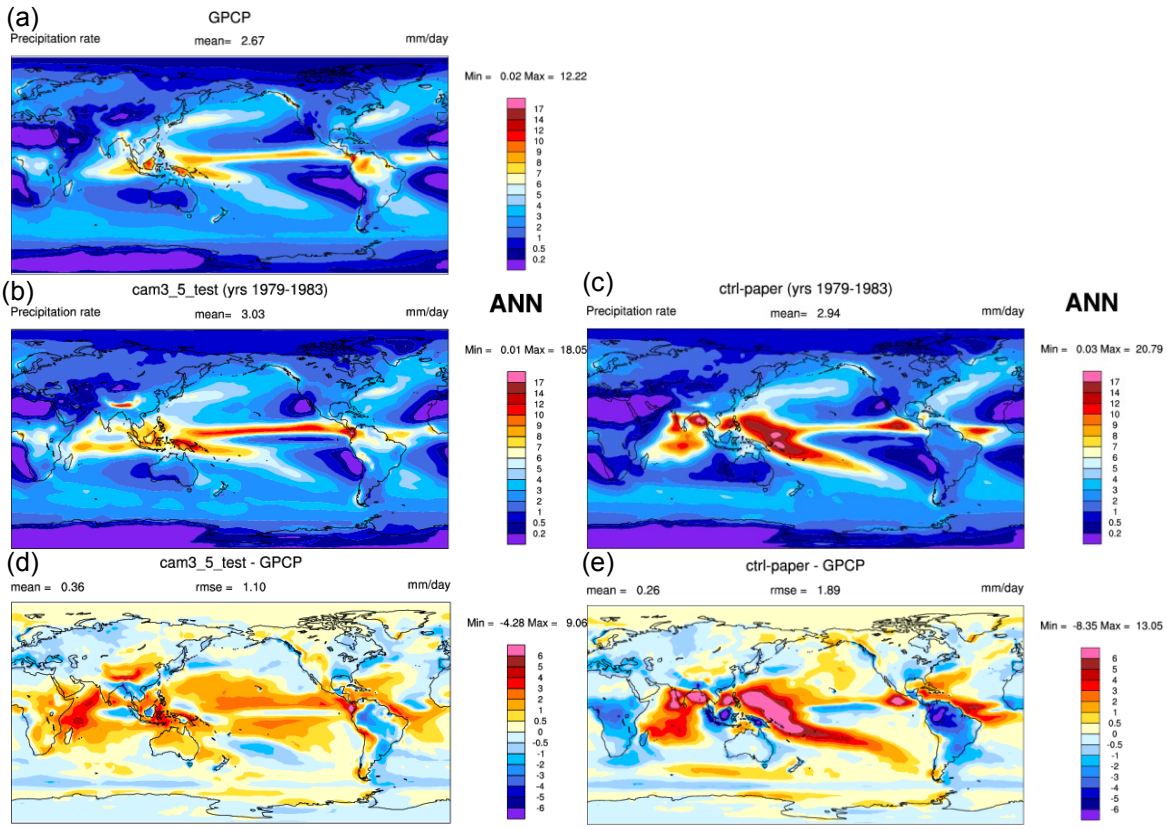

Figure 3.6. Precipitation simulated by CAM (b) and DEFAULT (c) and their bias ((d) and (e) compared with the GPCP observation (a).

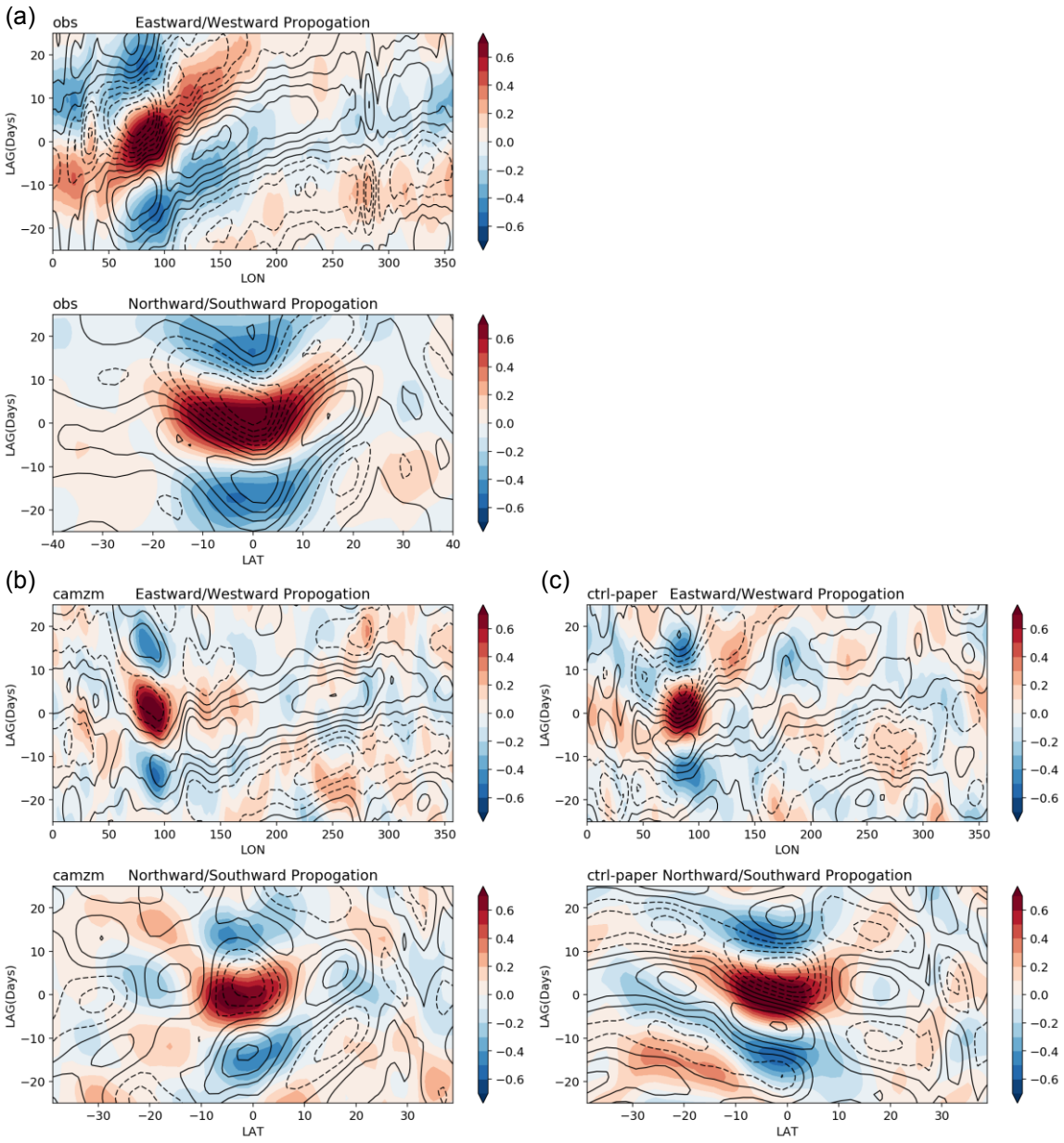

Figure 3.7 Lag-regression zonal mean (80°E to 100°E) and meridional mean (10°S to 10°N) of U850 (contour) and OLR (shading) upon the spatial average OLR within the reference area (from 10°S to 5°N, from 75°E to 100°E) for full seasons. All the results were converted to anomalies with a 20-100 day bandpass-filter before they were analyzed. (a) observation. (b) CAM. (c) DEFAULT.

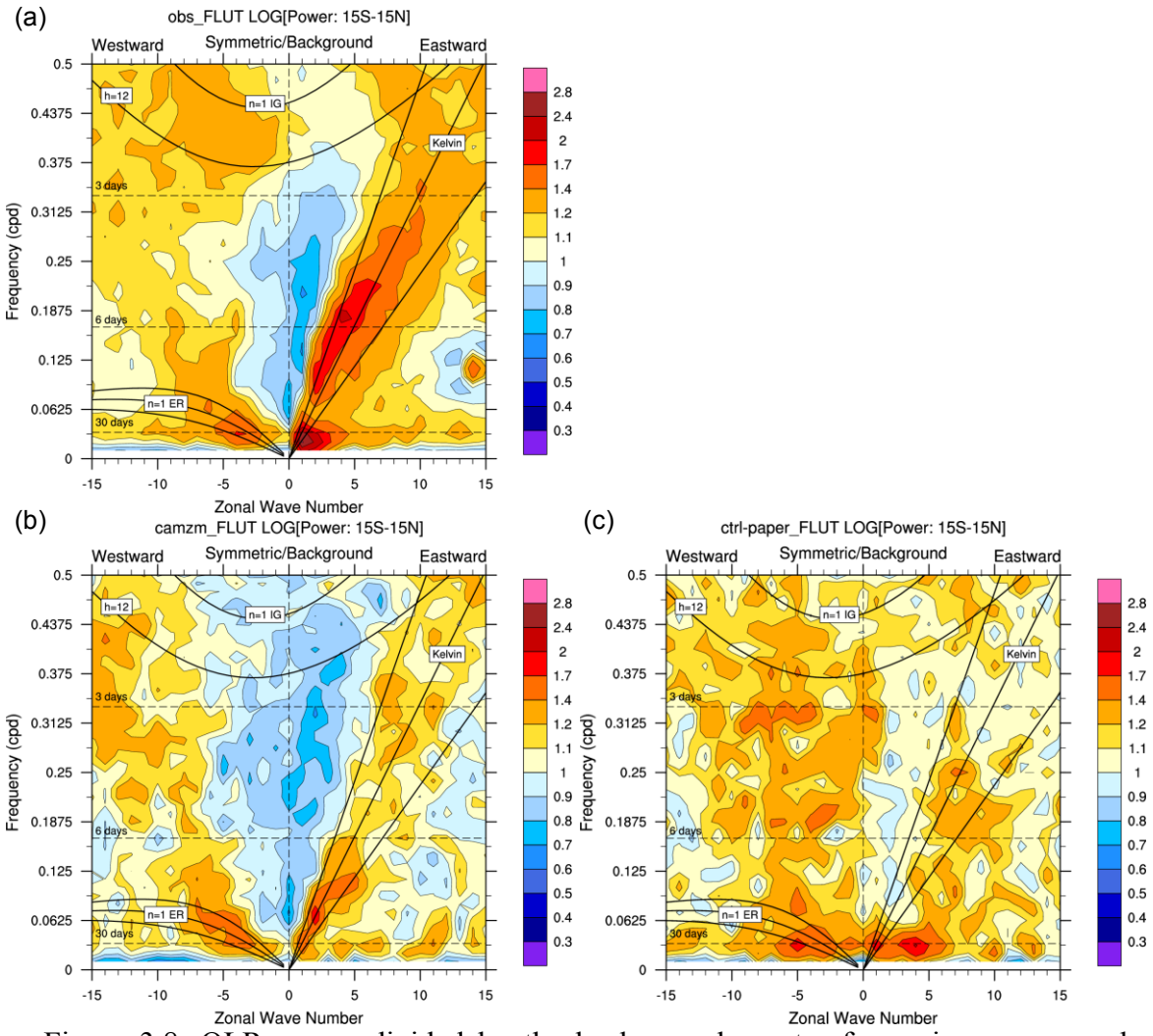

Figure 3.8. OLR power divided by the background spectra for various wavenumbers and frequencies in the tropics for (a) observation, (b) CAM and (c) DEFAULT.

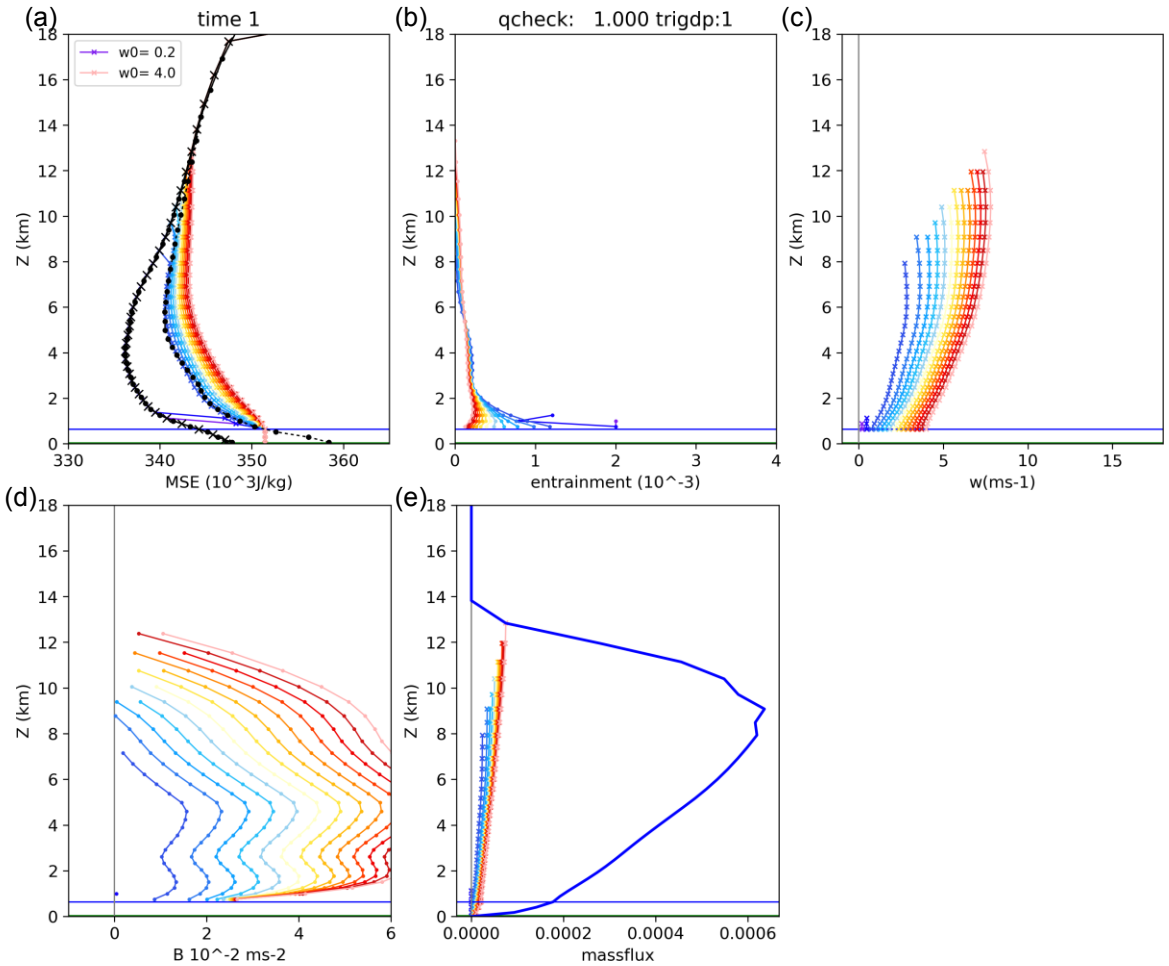

Figure 3.9. Same as Figure 3.1 but calculated with an initial vertical velocity range designed for deep convective plumes.

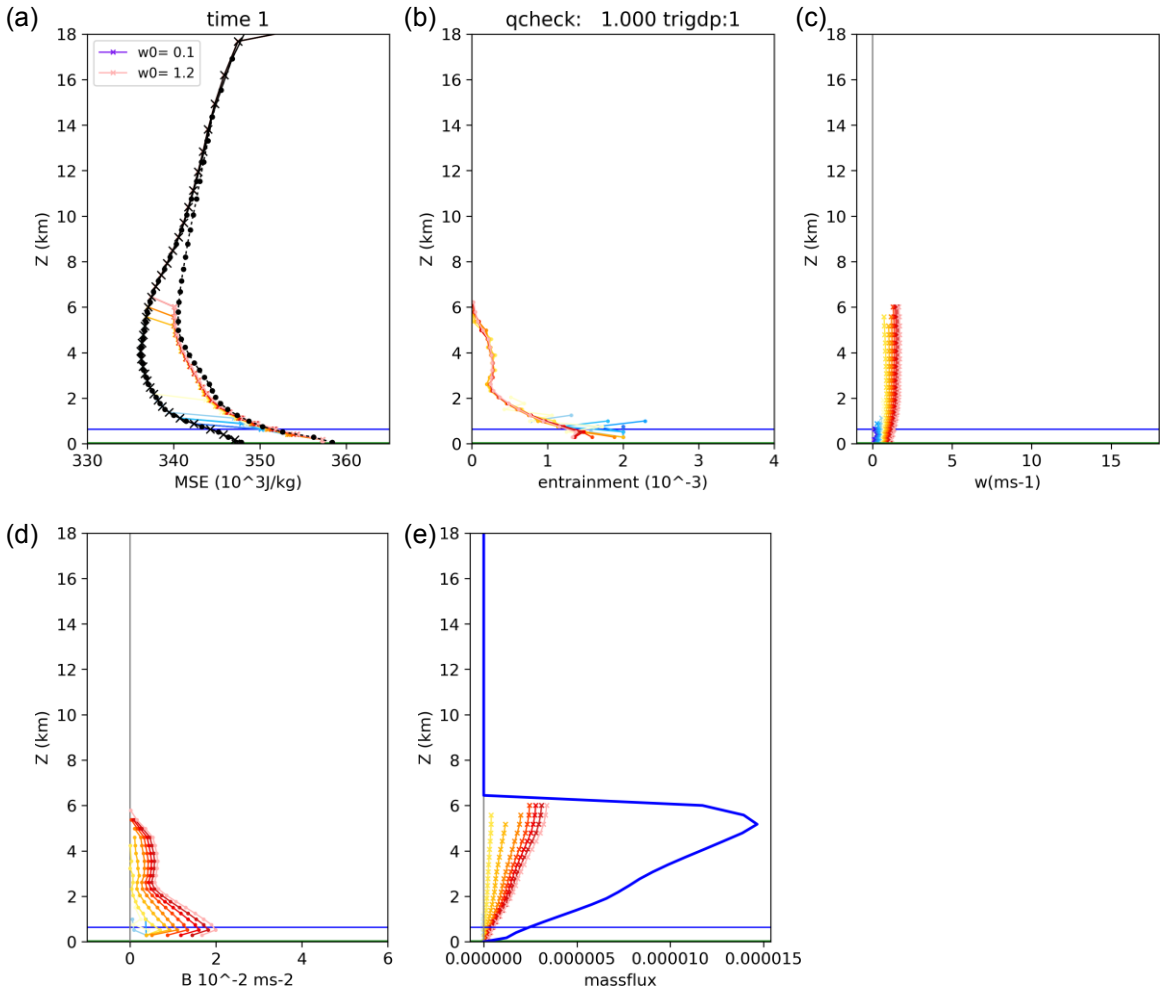

Figure 3.10. Same as Figure 3.1 but calculated with an initial vertical velocity range designed for shallow convective plumes.

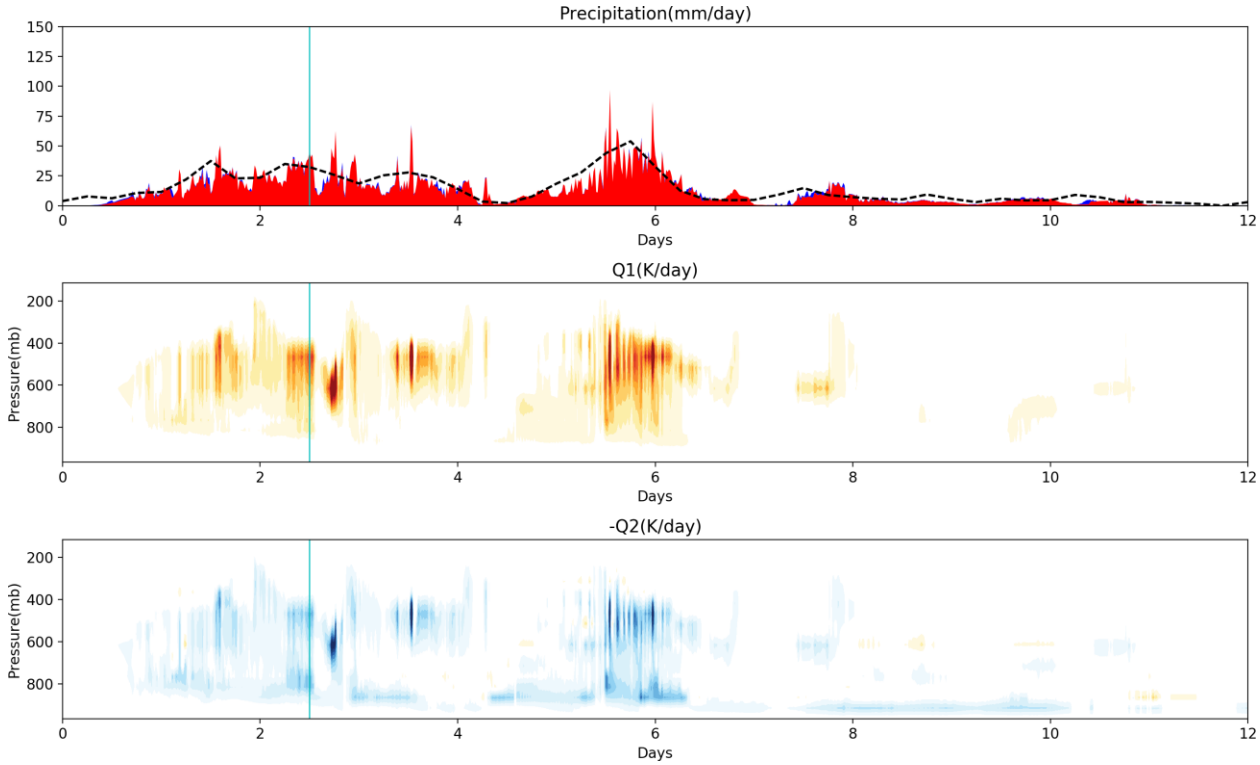

Figure 3.11. The TOGA-COARE case simulated by shallow plumes (SH). The figures are for precipitation, heating rate, and moistening rate, respectively.

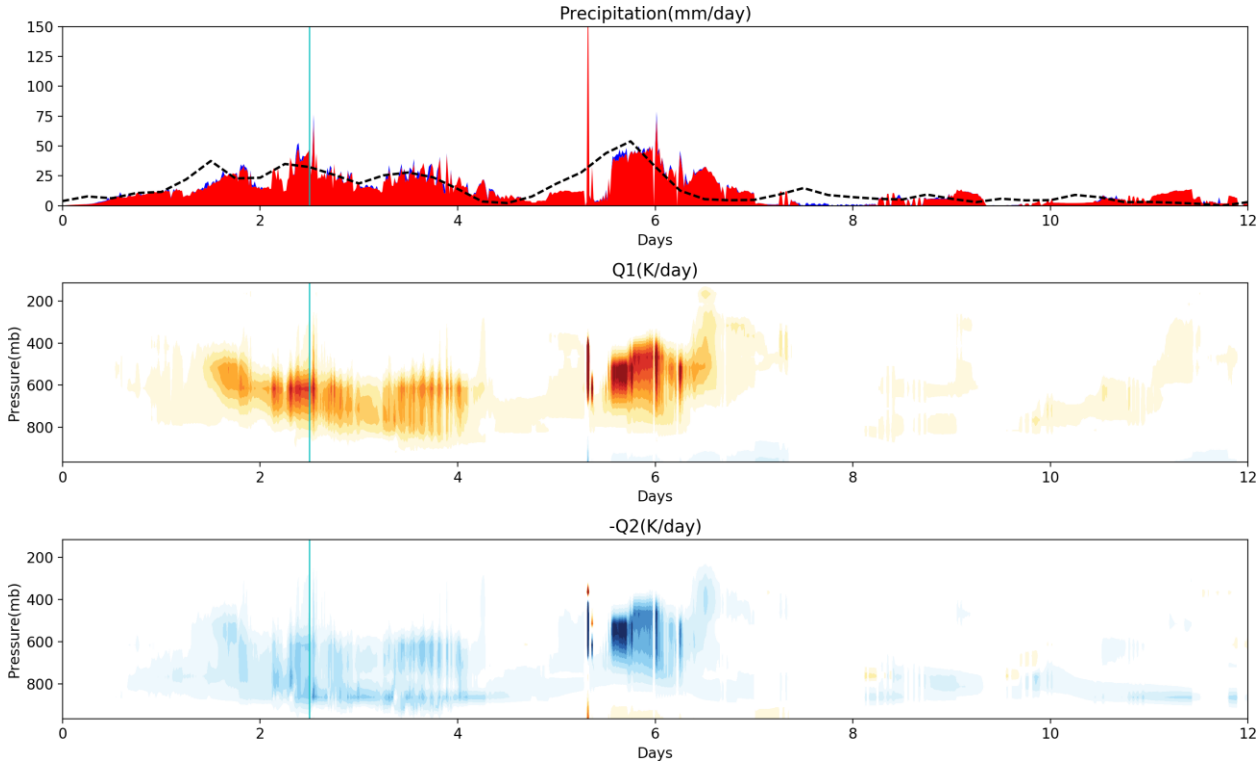

Figure 3.12. The TOGA-COARE case simulated by the deep plumes (DP). The figures are for precipitation, heating rate, and moistening rate, respectively.

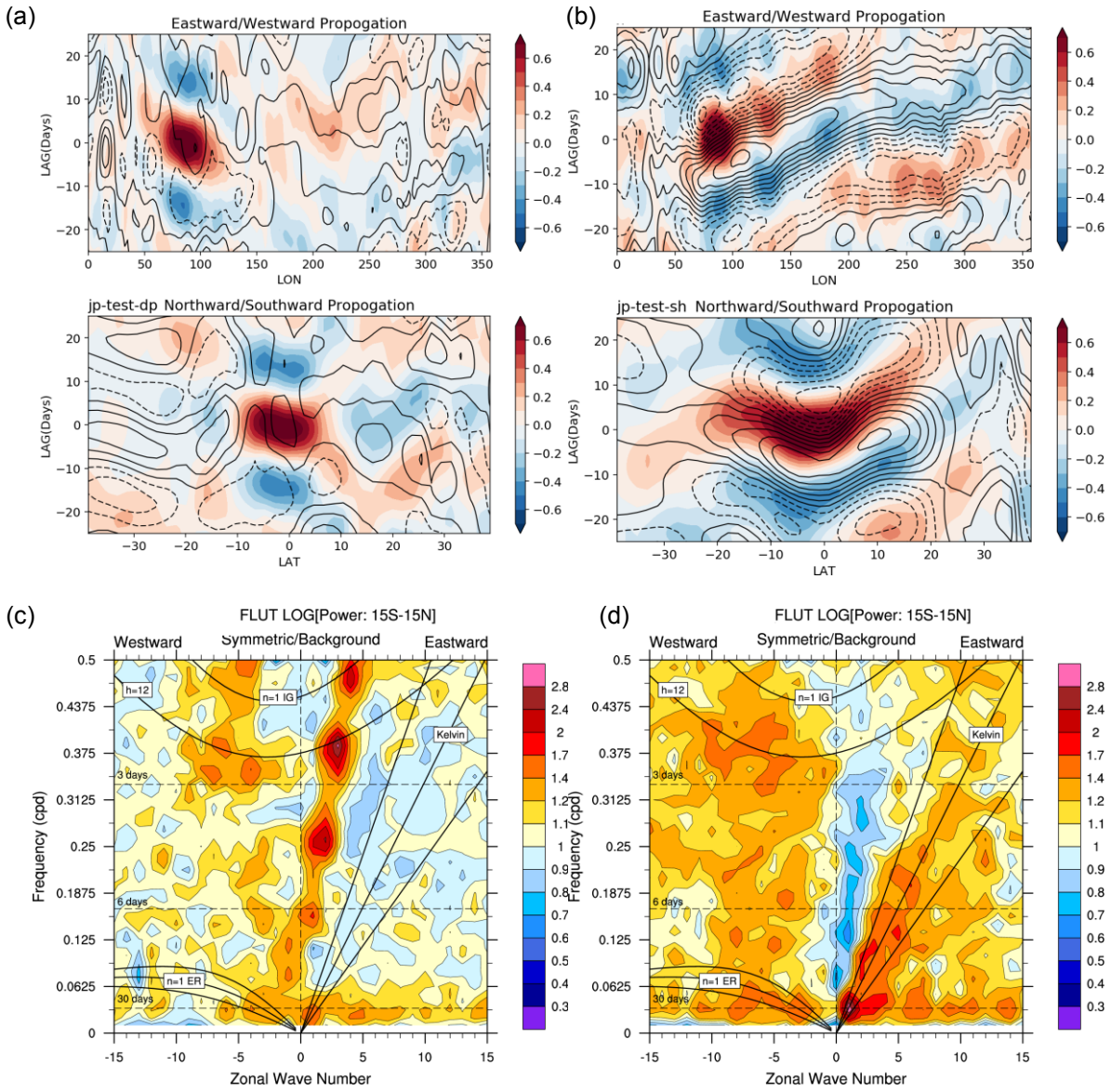

Figure 3.13. (a)(b) same as Figure 3.7 but using DP and SH respectively. (c)(d) same as Figure 3.8 but using DP and SH respectively.

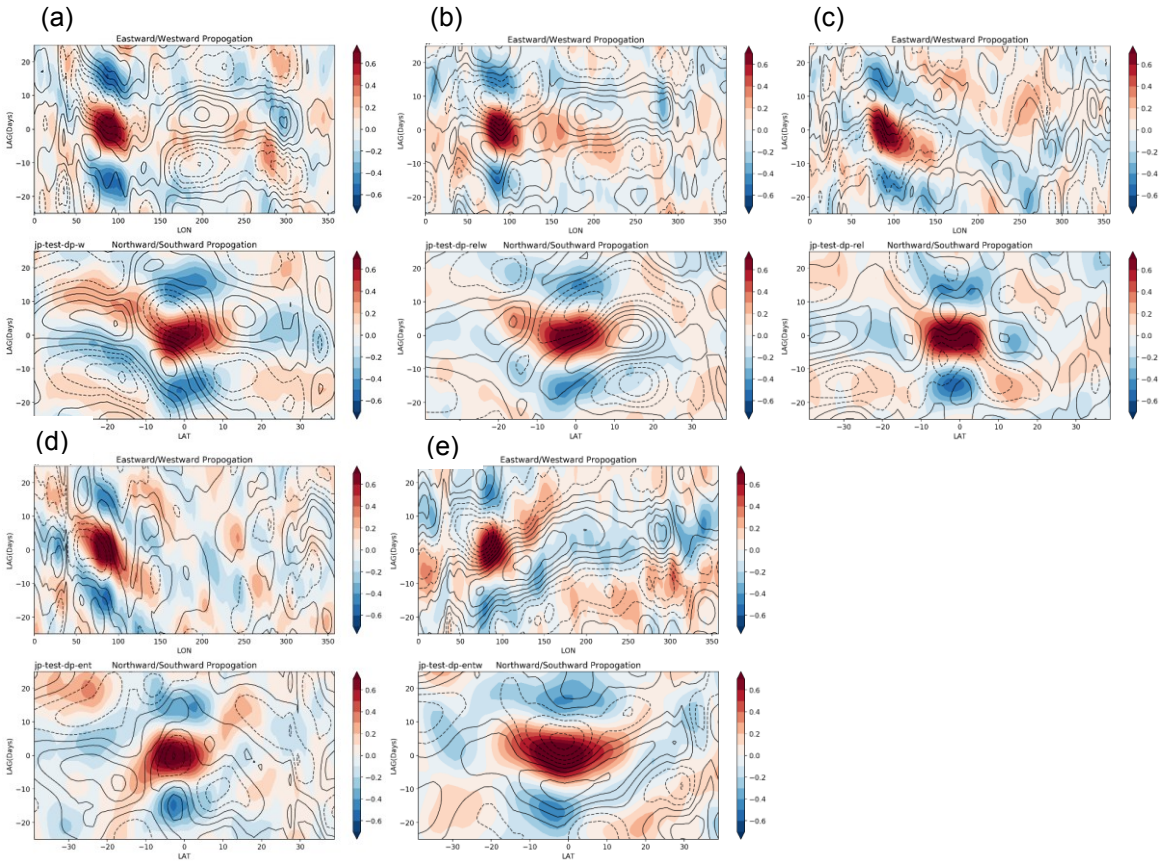

Figure 3.14. Lag regression plot same as Figure 3.7 but with different modifications applied to the DP. When all the modifications are applied, DP becomes SH. The launching level in all the cases here have been changed to the level of maximum MSE. (a) is with the change of initial vertical velocity range. (b) is with the change of both initial vertical velocity and dissipation time scale. (c) is with the improved dissipation time scale. (d) is with the change of entrainment parameter C_ε. (e) is with the change of both the entrainment parameter and the vertical velocity range.

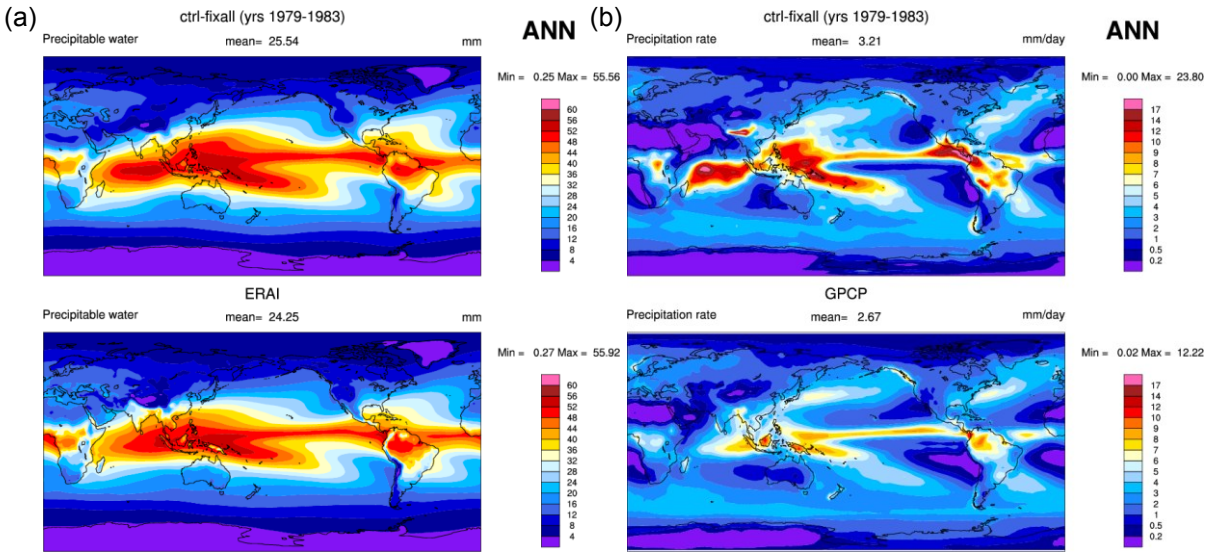

Figure 3.15. GCM simulation using the setting of the shallow plumes (upper panel) and observation (lower panel). (a) Precipitable water. (b) Total precipitation.

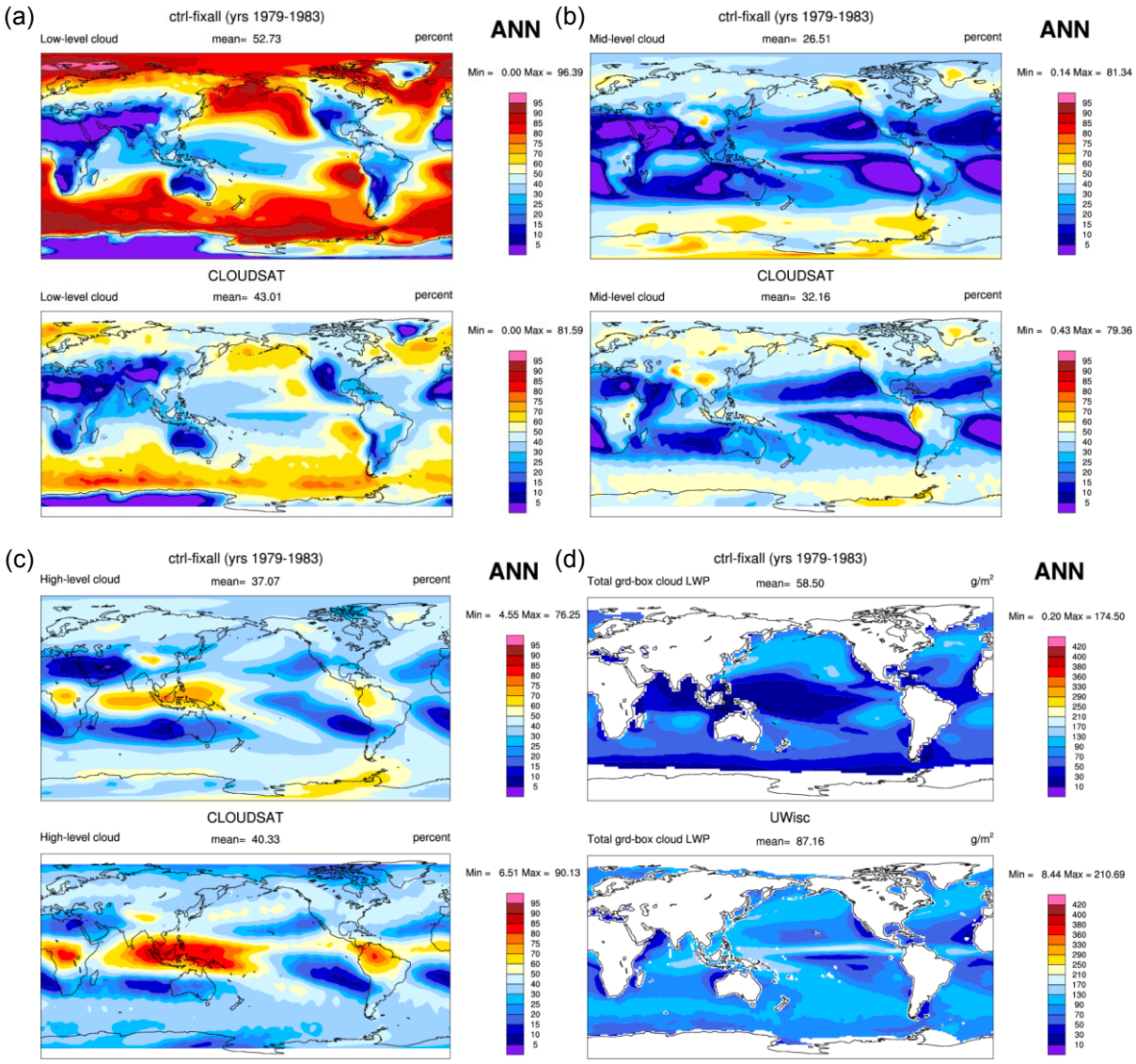

Figure 3.16. GCM simulation using the setting of the shallow plumes (upper panel) and observation (lower panel). (a) Low cloud. (b) Middle cloud. (c) High cloud. (d) Total grid-box cloud liquid water path.

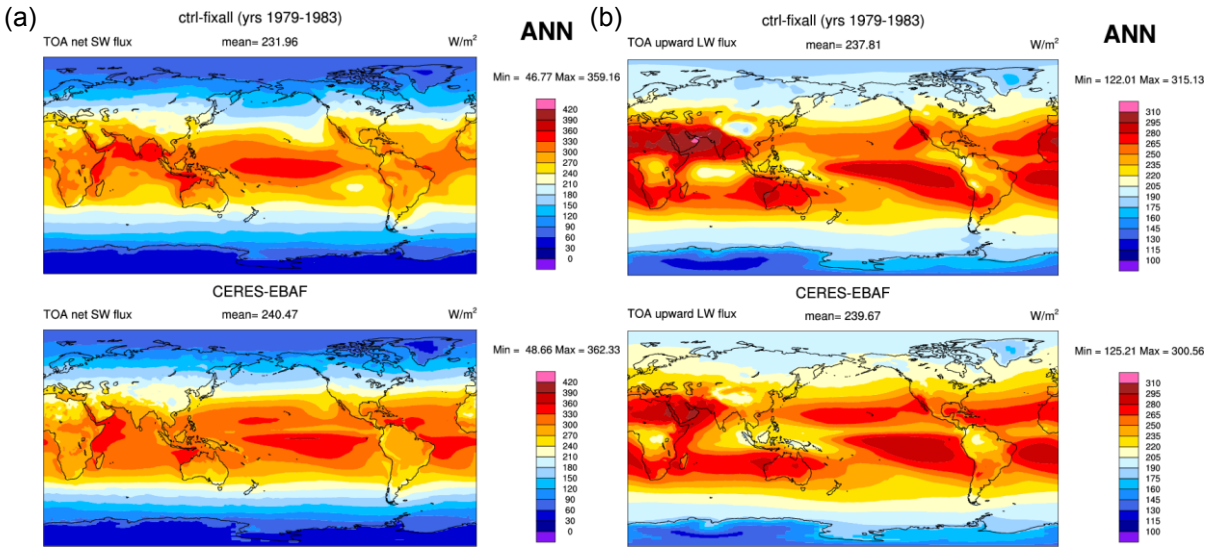

Figure 3.17. GCM simulation using the setting of the shallow plumes (upper panel) and observation (lower panel). (a) Net shortwave flux at TOA. (b) Upward longwave flux at TOA.

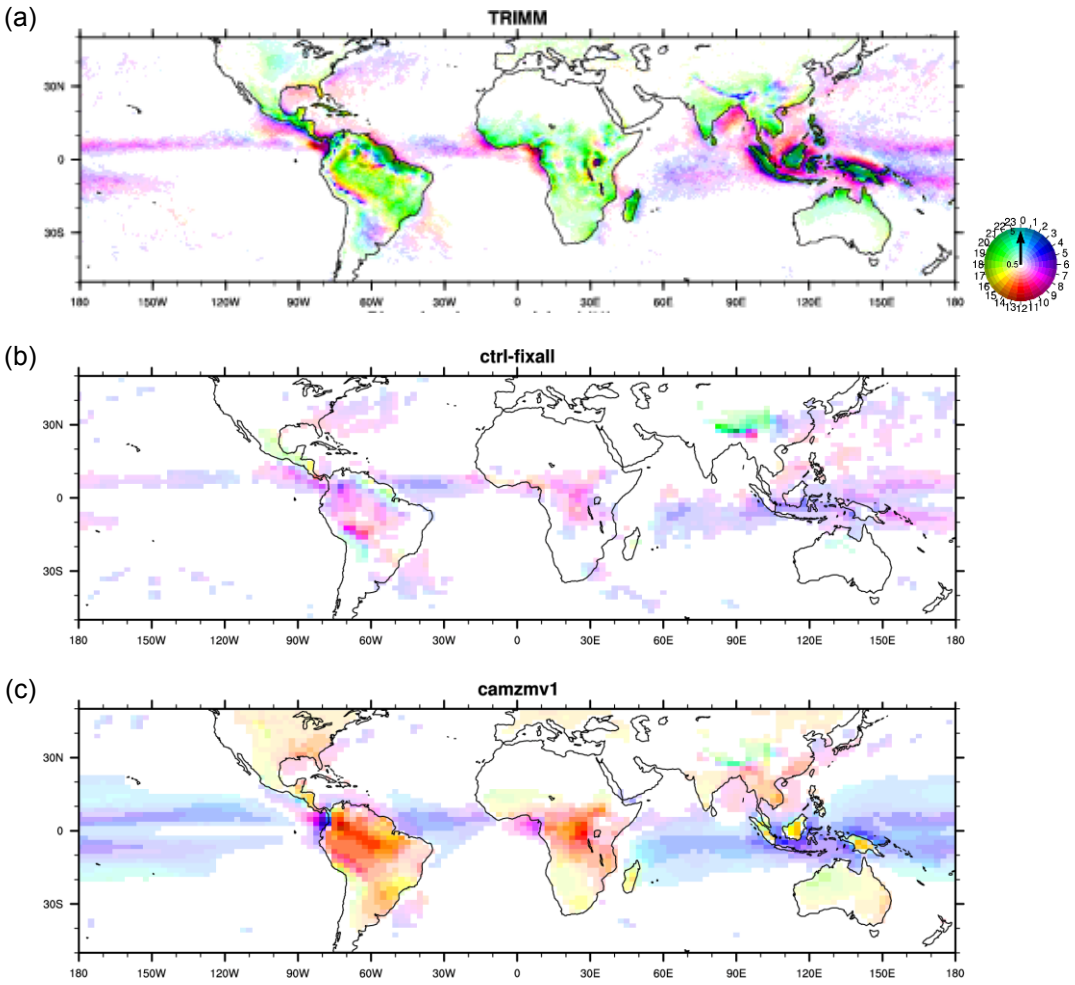

Figure 3.18. Diurnal cycle simulation performance. (a) Observation. (b) Simulation using the setting of shallow plumes. (c) Simulation using the CAM default version 1.2.1.

Chapter 4
Summary and Future Work

This dissertation has investigated the scale dependence of cloud liquid subgrid variability and its parameterization in a climate model. A convection parameterization with multiple plumes has been used to study the sensitivity of intraseasonal variability on the physical assumptions in the scheme.

4.1 Summary

We analyzed the long-term ground-based MICROBASE dataset to derive the liquid cloud inhomogeneity represented by the shape parameter ν of the Gamma distribution. Smaller ν is associated with larger inhomogeneity. We reported the dependence of ν on the horizontal scale and atmospheric instability and derived a scale-aware parameterization of ν that depends on the model resolution and atmospheric state.

The newly developed parameterization is implemented in CESM1. It provides the distribution of cloud liquid inhomogeneity to the microphysics scheme. Compared to the default CESM1, where a constant liquid inhomogeneity parameter was assumed, the scale-aware version reduces the cloud inhomogeneity at high latitudes and increases it at low latitudes. This is due to both the smaller grid size in high latitudes, and larger grid size in low latitudes in the longitude-latitude grid setting of CESM as well as the variation of the stability of the atmosphere. The single column model and GCM sensitivity experiments show that the new parameterization increases the cloud liquid water path in polar regions and decreases it in low latitudes.

Current CESM1 simulations suffer from the bias of both the pacific double-ITCZ precipitation and weak Madden-Julian oscillation (MJO). Previous studies show that convective parameterization with multiple plumes may alleviate such biases. A multiple-plume mass flux convective parameterization is implemented in CAM to investigate the sensitivity of MJO simulations. We show that MJO simulation is sensitive to entrainment rate specification, and shallow plumes play a key role in generating and sustaining the MJO propagation in the model.

4.2 Future Work

The scale-aware liquid cloud inhomogeneity parameterization we derived is only one component toward the scale-aware description of cloud microphysics. Future studies should include cloud ice and other hydrometeors. While the impact of the parameterized inhomogeneity on the simulated climate in this study is small, we think the main benefit of the scheme is its direct use in variable resolution models.

It would be also of interest to see what impact this scale-aware parameterization could bring when the model resolution increases to 1 degree or 0.5 degree since a full scale-aware model is meant to produce consistent results regardless of what resolution is used. From the equation 2.5, a generally smaller grid has less subgrid variability, and less adjusted autoconversion and accretion.

For the MJO sensitivity study, we have only chosen one formulation for the entrainment rate calculation in the multiple plume convection scheme. The specification of entrainment/detrainment rates and plume properties from other convective schemes can be used for more tests. Within the parameterization framework and implementation presented, new parameterizations of the closure scheme and precipitation properties can be tested and evaluated. Since we used a multiple plume parameterization, the plume properties solved by the scheme can also be compared with and constrained by results from cloud resolving models or observations.

Finally, further tuning work is needed for the current version of convection parameterization to simulate a better climatology given the results shown in Section 3.6. A common problem in tuning model is that climatology and variability performance seem to compromise each other. A better variability simulation such as MJO propagation usually results in a deterioration in climatology. Since in this study we have found the key components to the MJO simulation, a strategy is that we may change those sensitive parameters as less as possible while adjusting the other parameters until a better climatology is produced.

References

Arakawa, A., and W. H. Schubert (1974), Interaction of a Cumulus Cloud Ensemble with the Large-Scale Environment, Part I, *J Atmos Sci*, *31*(3), 674-701, doi: 10.1175/1520-0469(1974)031<0674:IOACCE>2.0.CO;2.

Barker, H. W. (1996), A parameterization for computing grid-averaged solar fluxes for inhomogeneous marine boundary layer clouds .1. Methodology and homogeneous biases, *Journal of the Atmospheric Sciences*, *53*(16), 2289-2303, doi: 10.1175/1520-0469(1996)053<2289:Apfcga>2.0.Co;2.

Barker, H. W., B. A. Wielicki, and L. Parker (1996), A parameterization for computing grid-averaged solar fluxes for inhomogeneous marine boundary layer clouds .2. Validation using satellite data, *J Atmos Sci*, *53*(16), 2304-2316, doi: 10.1175/1520-0469(1996)053<2304:Apfcga>2.0.Co;2.

Barker, H. W., G. L. Stephens, and Q. Fu (1999), The sensitivity of domain-averaged solar fluxes to assumptions about cloud geometry, *Quarterly Journal of the Royal Meteorological Society*, *125*(558), 2127-2152, doi: 10.1002/qj.49712555810.

Barker, H. W., J. N. S. Cole, J. J. Morcrette, R. Pincus, P. Räisänen, K. von Salzen, and P. A. Vaillancourt (2008), The Monte Carlo Independent Column Approximation: an assessment using several global atmospheric models, *Quarterly Journal of the Royal Meteorological Society*, *134*(635), 1463-1478, doi: 10.1002/qj.303.

Bechtold, P., M. Köhler, T. Jung, F. Doblas-Reyes, M. Leutbecher, M. J. Rodwell, F. Vitart, and G. Balsamo (2008), Advances in simulating atmospheric variability with the ECMWF model: From synoptic to decadal time-scales, *Quarterly Journal of the Royal Meteorological Society*, *134*(634), 1337-1351, doi: 10.1002/qj.289.

Bogenschutz, P. A., and S. K. Krueger (2013), A simplified PDF parameterization of subgrid-scale clouds and turbulence for cloud-resolving models, *Journal of Advances in Modeling Earth Systems*, *5*(2), 195-211, doi: 10.1002/jame.20018.

Boutle, I. A., S. J. Abel, P. G. Hill, and C. J. Morcrette (2013), Spatial variability of liquid cloud and rain: observations and microphysical effects, *Quarterly Journal of the Royal Meteorological Society*, n/a-n/a, doi: 10.1002/qj.2140.

Cahalan, R. F., W. Ridgway, W. J. Wiscombe, T. L. Bell, and J. B. Snider (1994), The Albedo of Fractal Stratocumulus Clouds, *J Atmos Sci*, *51*(16), 2434-2455, doi: 10.1175/1520-0469(1994)051<2434:TAOFSC>2.0.CO;2.

Chikira, M., and M. Sugiyama (2010), A Cumulus Parameterization with State-Dependent Entrainment Rate. Part I: Description and Sensitivity to Temperature and Humidity Profiles, *J Atmos Sci*, *67*(7), 2171-2193, doi: 10.1175/2010JAS3316.1.

Chikira, M., and M. Sugiyama (2013), Eastward-Propagating Intraseasonal Oscillation Represented by Chikira–Sugiyama Cumulus Parameterization. Part I: Comparison with Observation and Reanalysis, *J Atmos Sci*, *70*(12), 3920-3939, doi: 10.1175/JAS-D-13-034.1.

Gent, P. R., et al. (2011), The Community Climate System Model Version 4, *J. Climate*, *24*(19), 4973-4991, doi: 10.1175/2011JCLI4083.1.

Golaz, J.-C., V. E. Larson, and W. R. Cotton (2002), A PDF-Based Model for Boundary Layer Clouds. Part I: Method and Model Description, *J Atmos Sci*, *59*(24), 3540-3551, doi: 10.1175/1520-0469(2002)059<3540:APBMFB>2.0.CO;2.

Grützun, V., J. Quaas, C. J. Morcrette, and F. Ament (2013), Evaluating statistical cloud schemes: What can we gain from ground-based remote sensing?, *Journal of Geophysical Research: Atmospheres*, *118*(18), 10,507-510,517, doi: 10.1002/jgrd.50813.

Gregory, D. (2001), Estimation of entrainment rate in simple models of convective clouds, *Quarterly Journal of the Royal Meteorological Society*, *127*(571), 53-72, doi: 10.1002/qj.49712757104.

Hill, P. G., R. J. Hogan, J. Manners, and J. C. Petch (2012), Parametrizing the horizontal inhomogeneity of ice water content using CloudSat data products, *Quarterly Journal of the Royal Meteorological Society*, *138*(668), 1784-1793, doi: 10.1002/qj.1893.

Hogan, R. J., and A. J. Illingworth (2003), Parameterizing Ice Cloud Inhomogeneity and the Overlap of Inhomogeneities Using Cloud Radar Data, *J Atmos Sci*, *60*(5), 756-767, doi: 10.1175/1520-0469(2003)060<0756:PICIAT>2.0.CO;2.

Huang, D., and Y. Liu (2014), Statistical characteristics of cloud variability. Part II: Implication for parameterizations of microphysical and radiative transfer processes in climate models, *Journal of Geophysical Research: Atmospheres*, 2014JD022003, doi: 10.1002/2014JD022003.

Huang, D., E. Campos, and Y. Liu (2014), Statistical characteristics of cloud variability, Part I: Retrieved cloud liquid water path at three ARM sites, *Journal of Geophysical Research: Atmospheres*, 2014JD022001, doi: 10.1002/2014JD022001.

Jakob, C., and S. A. Klein (1999), The role of vertically varying cloud fraction in the parametrization of microphysical processes in the ECMWF model, *Quarterly Journal of the Royal Meteorological Society*, *125*(555), 941-965, doi: 10.1002/qj.49712555510.

Jakob, C., and S. A. Klein (2000), A parametrization of the effects of cloud and precipitation overlap for use in general-circulation models, *Quarterly Journal of the Royal Meteorological Society*, *126*(568), 2525-2544, doi: 10.1002/qj.49712656809.

Jess, S., P. Spichtinger, and U. Lohmann (2011), A statistical subgrid-scale algorithm for precipitation formation in stratiform clouds in the ECHAM5 single column model, *Atmos. Chem. Phys. Discuss.*, *11*(3), 9335-9374, doi: 10.5194/acpd-11-9335-2011.

Johnson, K., and M. Jensen (2011), Atmospheric Radiation Measurement (ARM) Climate Research Facility, Continuous Baseline Microphysical Retrieval (MICROBASEPI2), SGP C1, NSA C1, TWP C3, 2008 to 2010, doi: 10.5439/1034923.

Johnson, K., M. Dunn, and M. Jensen (2011), The Microbase Value-Added Product: A Baseline Retrieval of Cloud Microphysical Properties*Rep.*, Atmospheric Radiation Measurement Climate Research Facility.

Kawai, H., and J. Teixeira (2011), Probability Density Functions of Liquid Water Path and Total Water Content of Marine Boundary Layer Clouds: Implications for Cloud Parameterization, *Journal of Climate*, *25*(6), 2162-2177, doi: 10.1175/JCLI-D-11-00117.1.

Khairoutdinov, M., and Y. Kogan (2000), A new cloud physics parameterization in a large-eddy simulation model of marine stratocumulus, *Monthly Weather Review*, *128*(1), 229-243, doi: 10.1175/1520-0493(2000)128<0229:Ancppi>2.0.Co;2.

Khairoutdinov, M., and D. Randall (2001), A cloud resolving model as a cloud parameterization in the NCAR Community Climate System Model: Preliminary results, *Geophysical Research Letters*, *28*(18), 3617-3620, doi: 10.1029/2001GL013552.

Khairoutdinov, M., D. Randall, and C. DeMott (2005), Simulations of the Atmospheric General Circulation Using a Cloud-Resolving Model as a Superparameterization of Physical Processes, *J Atmos Sci*, *62*(7), 2136-2154, doi: 10.1175/JAS3453.1.

Larson, V. E., and J.-C. Golaz (2005), Using Probability Density Functions to Derive Consistent Closure Relationships among Higher-Order Moments, *Monthly Weather Review*, *133*(4), 1023-1042, doi: 10.1175/MWR2902.1.

Larson, V. E., and B. M. Griffin (2013), Analytic upscaling of a local microphysics scheme. Part I: Derivation, *Quarterly Journal of the Royal Meteorological Society*, *139*(670), 46-57, doi: 10.1002/qj.1967.

Lebsock, M., H. Morrison, and A. Gettelman (2013), Microphysical implications of cloud-precipitation covariance derived from satellite remote sensing, *Journal of Geophysical Research: Atmospheres*, *118*(12), 6521-6533, doi: 10.1002/jgrd.50347.

Li, C., X. Jia, J. Ling, W. Zhou, and C. Zhang (2009), Sensitivity of MJO simulations to diabatic heating profiles, *Climate Dynamics*, *32*(2), 167-187, doi: 10.1007/s00382-008-0455-x.

Lin, C., and A. Arakawa (1997), The Macroscopic Entrainment Processes of Simulated Cumulus Ensemble. Part I: Entrainment Sources, *J Atmos Sci*, *54*(8), 1027-1043, doi: 10.1175/1520-0469(1997)054<1027:TMEPOS>2.0.CO;2.

Lin, J. (2007), The Double-ITCZ Problem in IPCC AR4 Coupled GCMs: Ocean–Atmosphere Feedback Analysis, *Journal of Climate*, *20*(18), 4497-4525, doi: 10.1175/JCLI4272.1.

Lin, J., et al. (2006), Tropical Intraseasonal Variability in 14 IPCC AR4 Climate Models. Part I: Convective Signals, *Journal of Climate*, *19*(12), 2665-2690, doi: 10.1175/JCLI3735.1.

Madden, R. A., and P. R. Julian (1971), Detection of a 40–50 Day Oscillation in the Zonal Wind in the Tropical Pacific, *J Atmos Sci*, *28*(5), 702-708, doi: 10.1175/1520-0469(1971)028<0702:DOADOI>2.0.CO;2.

Morrison, H., and A. Gettelman (2008), A new two-moment bulk stratiform cloud microphysics scheme in the community atmosphere model, version 3 (CAM3). Part I: Description and numerical tests, *Journal of Climate*, *21*(15), 3642-3659, doi: 10.1175/2008jcli2105.1.

Norris, P. M., L. Oreopoulos, A. Y. Hou, W.-K. Tao, and X. Zeng (2008), Representation of 3D heterogeneous cloud fields using copulas: Theory for water clouds, *Quarterly Journal of the Royal Meteorological Society*, *134*(636), 1843-1864, doi: 10.1002/qj.321.

Oreopoulos, L., and R. F. Cahalan (2005), Cloud inhomogeneity from MODIS, *Journal of Climate*, *18*(23), 5110-5124, doi: 10.1175/Jcli3591.1.

Park, S. (2014), A Unified Convection Scheme (UNICON). Part I: Formulation, *J Atmos Sci*, *71*(11), 3902-3930, doi: 10.1175/JAS-D-13-0233.1.

Park, S., and C. S. Bretherton (2009), The University of Washington Shallow Convection and Moist Turbulence Schemes and Their Impact on Climate Simulations with the Community Atmosphere Model, *Journal of Climate*, *22*(12), 3449-3469, doi: 10.1175/2008JCLI2557.1.

Pincus, R., and S. A. Klein (2000), Unresolved spatial variability and microphysical process rates in large-scale models, *J Geophys Res-Atmos*, *105*(D22), 27059-27065, doi: 10.1029/2000jd900504.

Pincus, R., and B. Stevens (2009), Monte Carlo Spectral Integration: a Consistent Approximation for Radiative Transfer in Large Eddy Simulations, *Journal of Advances in Modeling Earth Systems*, *1*(2), 1, doi: 10.3894/JAMES.2009.1.1.

Pincus, R., S. A. McFarlane, and S. A. Klein (1999), Albedo bias and the horizontal variability of clouds in subtropical marine boundary layers: Observations from ships and satellites, *J Geophys Res-Atmos*, *104*(D6), 6183-6191, doi: 10.1029/1998jd200125.

Pincus, R., H. W. Barker, and J.-J. Morcrette (2003), A fast, flexible, approximate technique for computing radiative transfer in inhomogeneous cloud fields, *Journal of geophysical research*, *108*(D13), 4376, doi: 10.1029/2002JD003322.

Pincus, R., R. Hemler, and S. A. Klein (2006), Using Stochastically Generated Subcolumns to Represent Cloud Structure in a Large-Scale Model, *Monthly Weather Review*, *134*(12), 3644-3656, doi: 10.1175/MWR3257.1.

Raisanen, P., H. W. Barker, M. F. Khairoutdinov, J. N. Li, and D. A. Randall (2004), Stochastic generation of subgrid-scale cloudy columns for large-scale models, *Quarterly Journal of the Royal Meteorological Society*, *130*(601), 2047-2067, doi: 10.1256/Qj.03.99.

Shonk, J. K. P., and R. J. Hogan (2008), Tripleclouds: An Efficient Method for Representing Horizontal Cloud Inhomogeneity in 1D Radiation Schemes by Using Three Regions at Each Height, *Journal of Climate*, *21*(11), 2352-2370, doi: 10.1175/2007JCLI1940.1.

Shonk, J. K. P., and R. J. Hogan (2010), Effect of improving representation of horizontal and vertical cloud structure on the Earth's global radiation budget. Part II: The global effects, *Quarterly Journal of the Royal Meteorological Society*, *136*(650), 1205-1215, doi: 10.1002/qj.646.

Shonk, J. K. P., R. J. Hogan, J. M. Edwards, and G. G. Mace (2010), Effect of improving representation of horizontal and vertical cloud structure on the Earth's global radiation budget. Part I: Review and parametrization, *Quarterly Journal of the Royal Meteorological Society*, *136*(650), 1191-1204, doi: 10.1002/qj.647.

Simpson, J., and V. Wiggert (1969), Models of Precipitating Cumulus Towers, *Monthly Weather Review*, *97*(7), 471-&, doi: Doi 10.1175/1520-0493(1969)097<0471:Mopct>2.3.Co;2.

Slingo, J. M., et al. (1996), Intraseasonal oscillations in 15 atmospheric general circulation models: results from an AMIP diagnostic subproject, *Climate Dynamics*, *12*(5), 325-357, doi: 10.1007/BF00231106.

Stephens, G. L., P. M. Gabriel, and S.-C. Tsay (1991), Statistical radiative transport in one-dimensional media and its application to the terrestrial atmosphere, *Transport Theory and Statistical Physics*, *20*(2-3), 139-175, doi: 10.1080/00411459108203900.

Straka, J. M. (2009), *Cloud and Precipitation Microphysics: Principles and Parameterizations*.

Taylor, M. A., J. Edwalrds, and A. S. Cyr (2008), Petascale atmospheric models for the Community Climate System Model: new developments and evaluation of scalable dynamical cores, *J Phys Conf Ser*, *125*, 12023-12023, doi: 10.1088/1742-6596/125/1/012023.

Thom, H. C. S. (1958), A Note on the Gamma Distribution, *Monthly Weather Review*, *86*(4), 117-122, doi: 10.1175/1520-0493(1958)086<0117:ANOTGD>2.0.CO;2.

Tiedtke, M. (1989), A Comprehensive Mass Flux Scheme for Cumulus Parameterization in Large-Scale Models, *Monthly Weather Review*, *117*(8), 1779-1800, doi: 10.1175/1520-0493(1989)117<1779:ACMFSF>2.0.CO;2.

Tompkins, A. M. (2002), A Prognostic Parameterization for the Subgrid-Scale Variability of Water Vapor and Clouds in Large-Scale Models and Its Use to Diagnose Cloud Cover, *J Atmos Sci*, *59*(12), 1917-1942, doi: 10.1175/1520-0469(2002)059<1917:APPFTS>2.0.CO;2.

WALISER, D., et al. (2009), MJO Simulation Diagnostics, *Journal of Climate*, *22*(11), 3006-3030, doi: 10.1175/2008jcli2731.1.

Waliser, D. E., et al. (2003), AGCM simulations of intraseasonal variability associated with the Asian summer monsoon, *Climate Dynamics*, *21*(5), 423-446, doi: 10.1007/s00382-003-0337-1.

Weber, T., and J. Quaas (2012), Incorporating the subgrid-scale variability of clouds in the autoconversion parameterization using a PDF-scheme, *Journal of Advances in Modeling Earth Systems*, *4*(4), M11003, doi: 10.1029/2012MS000156.

Wood, R., P. R. Field, and W. R. Cotton (2002), Autoconversion rate bias in stratiform boundary layer cloud parameterizations, *Atmos Res*, *65*(1-2), 109-128, doi: 10.1016/S0169-8095(02)00071-6.

Xie, S., et al. (2010), CLOUDS AND MORE: ARM Climate Modeling Best Estimate Data, *Bulletin of the American Meteorological Society*, *91*(1), 13-20, doi: 10.1175/2009BAMS2891.1.

Xie, X., and M. Zhang (2015), Scale-aware parameterization of liquid cloud inhomogeneity and its impact on simulated climate in CESM, *Journal of Geophysical Research: Atmospheres*, *120*(16), 8359-8371, doi: 10.1002/2015JD023565.

Xu, K.-M. (1993), Cumulus ensemble simulation. The Representation of Cumulus Convection in Numerical Models, in *Meteorological Monographs*, edited by K. Emanuel, p. 246, American Meteorological Society.

Yanai, M., S. Esbensen, and J.-H. Chu (1973), Determination of Bulk Properties of Tropical Cloud Clusters from Large-Scale Heat and Moisture Budgets, *J Atmos Sci*, *30*(4), 611-627, doi: 10.1175/1520-0469(1973)030<0611:DOBPOT>2.0.CO;2.

Zhang, C. (2005), Madden-Julian Oscillation, *Reviews of Geophysics*, *43*(2), n/a-n/a, doi: 10.1029/2004RG000158.

Zhang, G., and N. A. McFarlane (1995), Sensitivity of climate simulations to the parameterization of cumulus convection in the Canadian climate centre general circulation model, *Atmosphere-Ocean*, *33*(3), 407-446, doi: 10.1080/07055900.1995.9649539.

Zhang, G., and X. Song (2009), Interaction of deep and shallow convection is key to Madden-Julian Oscillation simulation, *Geophysical Research Letters*, *36*(9), n/a-n/a, doi: 10.1029/2009GL037340.